1 **High Resolution 3D Winds Derived from a Modified WISSDOM Synthesis**
2 **Scheme using Multiple Doppler Lidars and Observations**
3
4
5
6

8 **Chia-Lun Tsai[1], Kwonil Kim[1], Yu-Chieng Liou[2], and GyuWon Lee*[1]**
9
10
11 [1]Department of Astronomy and Atmospheric Sciences, Center for Atmospheric REmote
12 sensing (CARE), Kyungpook National University, Daegu, South Korea
13
14 [2]Department of Atmospheric Sciences, National Central University, Jhongli, Taiwan

* Corresponding author: Prof. GyuWon Lee, E-mail: gyuwon@knu.ac.kr

Abstract

A WISSDOM (Wind Synthesis System using Doppler Measurements) synthesis scheme was developed to derive high-resolution 3-dimensional (3D) winds under clear-air conditions. From this variational-based scheme, detailed wind information was obtained from scanning Doppler lidars, automatic weather stations (AWS), sounding observations, and local reanalysis datasets (LDAPS, Local Data Assimilation and Prediction System), which were utilized as constraints to minimize the cost function. The objective of this study is to evaluate the performance and accuracy of derived 3D winds from this modified scheme. A strong wind event was selected to demonstrate its performance over complex terrain in Pyeongchang, South Korea. The size of the test domain is 12×12 km^2 extended up to 3 km height mean sea level (MSL) with remarkably high horizontal and vertical resolution of 50 m. The derived winds reveal that reasonable patterns were explored from a control run, as they have high similarity with the sounding observations. The results of intercomparisons show that the correlation coefficients between derived horizontal winds and sounding observations are 0.97 and 0.87 for u- and v-component winds, respectively, and the averaged bias (root mean square deviation, RMSD) of horizontal winds is between -0.78 and 0.09 (1.77 and 1.65) m s^{-1}. The correlation coefficients between WISSDOM-derived winds and lidar QVP (quasi-vertical profile) are 0.84 and 0.35 for u- and v-component winds, respectively, and the averaged bias (RMSD) of horizontal winds is between 2.83 and 2.26 (3.69 and 2.92) m s^{-1}. The statistical errors also reveal a satisfying performance of the retrieved 3D winds; the median values of wind directions are -5~5 (0~2.5) degrees, the wind speed is approximately -1~3 m s^{-1} (-1~0.5 m s^{-1}) and the vertical velocity is -0.2~0.6 m s^{-1} compared with the lidar QVP (sounding observations). A series of sensitivity tests with different weighting coefficients, radius of influence (RI) in interpolation and various combination of different datasets were also performed. The results indicate that the present setting of the control run is the optimal reference to WISSDOM synthesis in this event and will help verify the impacts against various scenarios and observational references in this area.

1. Introduction

In the past few decades, many practical methods have been developed to derive wind information by using meteorological radar data (Mohr and Miller, 1983, Lee et al., 1994, Liou and Chang, 2009, Bell et al. 2012). The derived winds substantially revealed reasonable patterns compared with conventional observations (such as surface stations, soundings, wind profiles, etc.) and models (Liou et al., 2014, North et al., 2017, Chen, 2019, Oue et al., 2019). Most comprehensive applications of the derived winds were adopted to document kinematic and precipitation structures associated with various weather systems or phenomena at different scales from thousands, hundreds, and a couple of kilometers, such as cold fronts, typhoons, tropical cyclone rainbands, convective lines, and nonprecipitation low-pressure systems (LPS) (Yu and Bond, 2002, Yu and Jou, 2005, Yu and Tsai, 2013, Yu and Tsai, 2017, Tsai et al. 2018, Yu et al., 2020, Cha and Bell, 2021, Tsai et al., 2022). In addition, the accuracy of 3D winds could be improved when increasing the numbers of Doppler radar because relatively fewer assumptions and more information can be included (Yu and Tsai 2010, Liou and Chang, 2009). Therefore, the retrieved schemes within multiple Doppler radars are a more popular way to obtain high-quality 3D winds and have been extensively applied to meteorological analyses.

The technique of velocity track display (VTD, Lee et al., 1994) and ground-based velocity track display (GBVTD, Lee et al., 1999) can derive the winds from single Doppler radar under some assumptions, as the wind patterns are generally uniform or axisymmetric rotational (Cha and Bell, 2021). More extended techniques based on VTD and GBVTD have also been applied to increase the quality of derived wind data, and such techniques include Extended-GBVTD (EGBVTD, Liou et al., 2006) and generalized velocity track display (GVTD, Jou et al., 2008). However, winds usually present nonuniform patterns and fast-evolving characteristics in most mesoscale weather systems and microscale phenomena, and complete and detailed winds are still difficult to resolve by these techniques. Most developed techniques are based on the contexts of weaknesses from the above schemes on wind retrievals. Instead of a single Doppler radar,

68 multiple Doppler can retrieve better quality 3D winds with relativity fewer assumptions because

69 they provide sufficient radial velocity measurements and wind information with wider coverage

70 in the synthesis domain.

71   Cartesian Space Editing, Synthesis, and Display of Radar Fields under Interactive Control

72 (CEDRIC, Mohr and Miller, 1983) is a traditional package used to retrieve 3D winds by dual-

73 Doppler radar observations. This scheme usually determines the horizontal winds by using two

74 radars, and the vertical velocity can be obtained by variational adjustment with anelastic

75 continuity equation. Spline Analysis at Mesoscale Utilizing Radar and Aircraft Instrumentation

76 (SAMURAI) software is another way to retrieve 3D winds (Bell et al., 2012); this scheme is a

77 kind of variational data assimilation that adopts multiple radars. Recently, Tsai et al. (2018)

78 utilized the measurements of six Doppler radars to document precipitation and airflow structures

79 over complex terrain on the northeastern coast of South Korea via WISSDOM (Wind Synthesis

80 System using Doppler Measurements). Liou and Chang (2009) is the first purposes of this

81 algorithm. Furthermore, they performed immersed boundary method (IBM, Tseng and Ferziger,

82 2003) in WISSDOM, and its scientific applications were documented in Liou et al. (2012) and

83 Liou et al. (2016), respectively. Since one of the advantages of WISSDOM is that it considers

84 the orographic forcing on Cartesian coordinates by applying the IBM, higher quality 3D winds

85 can be derived well over terrain (Liou et al., 2013, 2014, Lee et al., 2018).

86   Generally, radial velocity is measured by detecting the movement of precipitation particles

87 relative to the locations of Doppler radars; thus, there are no sufficient radial velocity

88 measurements under clear-air conditions. However, the winds in clear-air conditions usually play

89 an important role in the initiations of various weather systems and phenomena, such as downslope

90 winds, gap winds, and wildfires (Reed, 1931, Colle and Mass, 2000, Mass and Ovens, 2019, Lee

91 et al., 2020). Although surface stations, soundings, and wind profilers can measure winds under

92 clear-air conditions, relatively poor spatial coverage is still a problem for obtaining sufficient

93 wind information in certain local areas. Therefore, scanning Doppler lidars will be one approach

to obtain wind information under clear-air conditions. Päschke et al. (2015) assessed the quality of wind derived by Doppler lidar with a wind profiler in a year trial, and the results showed good agreement in wind speed (the error ranged between 0.5 and 0.7 m s^{-1}) and wind direction (the error ranged between 5° and 10°). Bell et al. (2020) combined an intersecting range height indicator (RHI) of six Doppler lidars to build "virtual towers" (such as wind profilers) to investigate the airflow over complex terrain during the Perdigão experiment. These virtual towers can fill the gap in wind measurements above meteorological towers. The uncertainty of wind fields is also reduced by adopting multiple Doppler lidars (Choukulkar et al., 2017), and a high spatiotemporal resolution of derived wind is allowed to check small-scale rotors in mountainous areas (Hill et al., 2010).

The original WISSDOM was designed to retrieve 3D winds based on Doppler radar observations and background inputs combined with conventional observations and modeling. However, the original WISSDOM only provided 3D winds under precipitation conditions. It does not work well under clear-air conditions because Doppler radar cannot easily detect radial velocity without precipitation particles. To obtain high-quality 3D winds under clear-air conditions, the radial velocity observed from the scanning Doppler lidars can be used in modified WISSDOM. The results will allow us to investigate the initiations of precipitation systems in advance of rainfall and snowfall, which is an essential benefit rather than Doppler radar in related research topics. Furthermore, the conventional observations and modeling datasets were used as isolated constraints in the modified WISSDOM synthesis scheme. One of the benefits of the isolated constraints is that it is easy to synthesize any kind of wind information obtained from available datasets and give suitable weighting coefficients with different constraints when they are processing the minimization in the cost function. Thus, more reliable 3D winds in clear-air conditions were well derived from this modified WISSDOM synthesis scheme.

The objective of this study is to modify the WISSDOM synthesis scheme based on the original version to be a more flexible and useful scheme by adding any number of Doppler lidars

120   and conventional observations as well as modeling datasets. This modified WISSDOM will allow

121   us to obtain an exceedingly high spatial resolution of 3D winds (50 m was set in this study) under

122   clear-air conditions. A resolution of 50 m was chosen in this study, as the Doppler lidars'

123   respective horizontal resolution averages 40-60 m. A variety of adequate datasets were collected

124   during a strong wind event in the winter season during an intensive field experiment ICE-POP

125   2018 (International Collaborative Experiments for Pyeongchang 2018 Olympic and Paralympic

126   winter games). In summary, the main goal of this study is to use Doppler lidar observations to

127   retrieve high-resolution 3D winds over terrain with clear-air conditions via WISSDOM. In this

128   study, detailed principles of the modified WISSDOM and data implementation are elucidated in

129   the following sections. In addition, the modified WISSDOM was performed to retrieve 3D winds

130   over complex terrain under clear-air conditions in a strong wind event. The reliability of the

131   derived 3D winds was also evaluated and discussed with conventional observations.

132   **2. Methodology**

133   **2.1 Original version of WISSDOM (WInd Synthesis System using DOppler Measurements)**

134   WISSDOM is a mathematically variational-based scheme to minimize the cost function, and

135   various wind-related observations can be used as one of the constraints in the cost function. The

136   3D winds were derived by variationally adjusted solutions to satisfy the constraints in the cost

137   function; thus, this is a gradient decent technique to converge toward a solution. The original

138   version of WISSDOM performed five constraints, including radar observations (i.e., reflectivity

139   and radial velocity), background (combined with automatic weather stations, sounding, model or

140   reanalysis data), continuity equation, vorticity equation, and Laplacian smoothing (Liou and

141   Chang 2009). Liou et al. (2012) applied the IBM in WISSDOM to consider the effect on the

142   nonflat surfaces. One of the advantages of IBM is providing realistic topographic forcing without

143   changing the Cartesian coordinate system into a terrain-following coordinate system. More

144   scientific documentation associated with the interactions between terrain, precipitation, and

145   winds in different areas can be found in Liou et al. (2016) for Taiwan and in Tsai et al. (2018) for

146   South Korea. The cost function can be expressed as

147
$$J = \sum_{M=1}^{5} J_M, \tag{1}$$

148   where J_M is the different constraints. J_1 is the constraint related to the geometric relation

149   between radar radial Doppler velocity observations (V_r) and derived one from true winds $(\mathbf{V}_t =$

150     $u_t \mathbf{i} + v_t \mathbf{j} + w_t \mathbf{k})$ in Cartesian coordinates [eq. (2)]. Note that the $\mathbf{V}_t$ will be first guessed,

151   resulting from the background of the sounding observations used in this study.

152
$$J_1 = \sum_{t=1}^{2} \sum_{x,y,z} \sum_{i=1}^{N} \alpha_{1,i} \left(T_{1,i,t} \right)^2. \tag{2}$$

153   Since WISSDOM is a scheme that uses the 4DVAR approach, the variations between different

154   time steps (t) should be considered, and two time steps of radar observations were collected in

155   this constraint and all following constraints. The x, y, z indicates the locations of a given grid

156   point in the synthesis domain, and i could be any number (N) of radars (at least 1). The α_1 is

157   the weighting coefficient of J_1 (α_2 is the weighting coefficient of J_2 and so on). $T_{1,i,t}$ in eq.

158   (2) is defined as eq. (3):

159
$$T_{1,i,t} = (V_r)_{i,t} - \frac{(x - P_x^i)}{r_i} u_t - \frac{(y - P_y^i)}{r_i} v_t - \frac{(z - P_z^i)}{r_i} (w_t - W_{T,t}), \tag{3}$$

160     $(V_r)_{i,t}$ is the radial velocity observed by the radar (i) at time step (t), P_x^i, P_y^i and P_z^i depict the

161   coordinate of radar i. The u_t, v_t and w_t $(W_{T,t})$ denote the 3D winds (terminal velocity of

162   precipitation particles) at given grid points at the time step t ; and $r_i =$

163     $\sqrt{(x - P_x^i)^2 + (y - P_y^i)^2 + (z - P_z^i)^2}$.

164   The second constraint is the difference between the background $(\mathbf{V}_{B,t})$ and true (derived)

165   wind field $(\mathbf{V}_t = u_t \mathbf{i} + v_t \mathbf{j} + w_t \mathbf{k})$, which is defined as

166
$$J_2 = \sum_{t=1}^{2} \sum_{x,y,z} \alpha_2 \left(\mathbf{V}_t - \mathbf{V}_{B,t} \right)^2 . \tag{4}$$

167   There were several options to obtain background in the original version of WISSDOM. The most

168   popular background resource involves using sounding observations; however, it can only provide

169   homogeneous wind information for each level in WISSDOM with relatively coarse temporal

170   resolution (3- to 12-hour intervals). The other option is combining sounding observations with

171   AWS (automatic weather station) observations. Although the AWS provided wind information

172   with better temporal resolution (1-min), the data were only observed at the surface layer with

173   semirandom distributions. The last option is to combine sounding, AWS, modeling or reanalysis

174   datasets. However, various datasets with different spatiotemporal resolutions are not favorable

175   for appropriate interpolation of given grid points of WISSDOM synthesis, and the accuracy and

176   reliability of the background may have been significantly affected by such a variety of datasets.

177   Thus, these different observed or model data should be treated differently to minimize

178   uncertainties and improve accuracy. Therefore, one of the improvements in the modified

179   WISSDOM is that these inputs were individually separated into independent constraints with

180   flexible interpolation methods. In addition, individual constraints considered the time if the

181   temporal resolution of the inputs was equal to or higher than the time interval of the WISSDOM

182   outputs. Note that the sounding observations are still a necessary dataset because the air density

183   and temperature profile were used to identify the height of the melting level. In this study,

184   sounding winds were adopted to represent the background for each level and a constraint at the

185   same time; nevertheless, the AWS and reanalysis dataset are independent constraints in the

186   modified WISSDOM (details are provided in the following section).

187   The third, fourth and fifth constraints in the cost function are the anelastic continuity

188   equation, vertical vorticity equation and Laplacian smoothing filter, respectively. Equations (5),

189   (6) and (7) are denoted as follows:

$$190 \quad J_3 = \sum_{t=1}^{2} \sum_{x,y,z} \alpha_3 \left[\frac{\partial(\rho_0 u_t)}{\partial x} + \frac{\partial(\rho_0 v_t)}{\partial y} + \frac{\partial(\rho_0 w_t)}{\partial z} \right]^2, \qquad (5)$$

$$191 \quad J_4 = \sum_{x,y,z} \alpha_4 \left\{ \frac{\partial \zeta}{\partial t} + \overline{\left[u\frac{\partial \zeta}{\partial x} + v\frac{\partial \zeta}{\partial y} + w\frac{\partial \zeta}{\partial z} + (\zeta + f)\left(\frac{\partial u}{\partial x} + \frac{\partial v}{\partial y} \right) + \left(\frac{\partial w}{\partial x}\frac{\partial v}{\partial y} - \frac{\partial w}{\partial y}\frac{\partial u}{\partial z} \right) \right]} \right\}^2, \quad (6)$$

$$192 \quad J_5 = \sum_{t=1}^{2} \sum_{x,y,z} \alpha_5 [\nabla^2 (u_t + v_t + w_t)]^2. \qquad (7)$$

193   ρ_0 in eq. (5) is the air density, and $\zeta = \partial v/\partial x - \partial u/\partial y$ in eq. (6). The main advantage is that

194   using vertical vorticity can provide further improvement in winds and thermodynamic retrievals

195   from a method named as Terrain-Permitting Thermodynamic Retrieval Scheme (TPTRS, Liou et

196   al. 2019).

2.2 The modified WISSDOM

198   In addition to the five constraints in the original version, the modified WISSDOM synthesis

199   scheme includes three more constraints in the cost function. Thus, the cost function in the

200   modified WISSDOM was written as

$$201 \quad J = \sum_{M=1}^{8} J_M. \qquad (8)$$

202    $J_1 \sim J_5$ in (8) are the same constraints corresponding to equations (2)-(7). The main purpose

203   of this study is to retrieve 3D winds under clear-air conditions in which observational data are

204   relatively rare. Instead of the radial velocity $(V_r)_{i,t}$ observed from Doppler radars in eq. (3) in

205   original version of WISSDOM, the radial velocity observed from Doppler lidars was adopted in

206   the modified WISSDOM synthesis. In addition, if there were no precipitation particles under

207   clear-air conditions, the terminal velocity of precipitation particles $(W_{T,t})$ was set to zero in eq.

208   (3) in the modified WISSDOM. In this study, the time steps in WISSDOM were set by the

209   synthesis time and 12 mins before the synthesis time due to the temporal resolution of the primary

210   input lidar data being 12 mins. Notably, relatively minor changes in environmental conditions

211   were assumed in WISSDOM due to the limitation on the coarse temporal resolution from specific

212   inputs. For example, the closest time step of a sounding observation or LDAPS dataset was

213   chosen regarding the synthesis time, and the time constrain was set to be the same.

214   The sixth constraint is the difference between the derived wind fields and the sounding

215   observations ($\mathbf{V}_{S,t}$), as defined in (9):

216
$$J_6 = \sum_{t=1}^{2} \sum_{x,y,z} \alpha_6 \left(V_t - V_{S,t} \right)^2. \tag{9}$$

217   The sounding data in J_6 were interpolated to the given grid points near its tracks bearing on the

218   radius influence (RI) distance (the details are provided in Section 3.2.3). The main difference

219   between J_6 and J_2 is that the sounding data with various wind speeds and directions were used

220   as an observation for given 3D locations in J_6 instead of the constraint of homogeneous

221   background winds (i.e., uniform wind speed and direction) for each level in the studied domain

222   in J_2. An additional benefit of J_6 is that any number of sounding observations can be efficiently

223   adopted in the WISSDOM synthesis domain. The seventh constraint represents the discrepancy

224   between the true (derived) wind fields and AWS ($\mathbf{V}_{A,t}$), as expressed in (10):

225
$$J_7 = \sum_{t=1}^{2} \sum_{x,y,z} \alpha_7 \left(V_t - V_{A,t} \right)^2. \tag{10}$$

226   Finally, the eighth constraint measures the misfit between the derived winds and the local

227   reanalysis dataset ($\mathbf{V}_{L,t}$), as defined in (11):

228
$$J_8 = \sum_{t=1}^{2} \sum_{x,y,z} \alpha_8 \left(V_t - V_{L,t} \right)^2. \tag{11}$$

229   In this study, various observations and reanalysis datasets were utilized as constraints in the cost

230   function of WISSDOM. The most important dataset is the radial velocity observed from Doppler

231   lidars, which can measure wind information with high spatial resolution and good coverage from

232   near the surface up to higher layers in the test domain. Sounding and AWS can provide horizontal

233   winds for background or to be included in the constraints. The local reanalysis datasets were

234   obtained from the 3DVAR Local Data Assimilation and Prediction System (LDAPS) data

235   assimilation system from the Korea Meteorological Administration (KMA). Since these datasets

236   have different coordinate systems and various spatiotemporal resolutions, additional procedures

237   are required before the synthesis. Detailed descriptions of the procedures are described in the next

238   section.

239   The high-quality synthesized 3D wind field from radar observations has been applied in

240   several previous studies such as those by Liou and Chang (2009), Liou et al. (2012, 2013, 2014,

241   2016), and Lee et al. (2017). The advantages and details of the WISSDOM can be found in Tsai

242   et al. (2018). Although several studies have used Doppler radar in WISSDOM, this study is the

243   first time to apply Doppler lidar data in WISSDOM. This modified WISSDOM synthesis scheme

244   has also been applied in the analysis related to the mechanisms of orographically induced strong

245   wind on the northeastern coast of Korea (Tsai et al., 2022). In contrast to previous studies, this

246   study provides clear context, detailed procedures, reliability, and the limitations of the modified

247   WISSDOM.

248   **3. Data processing with a strong wind event**

249   **3.1 Basic information of WISSDOM synthesis**

250   A small domain near the northeastern coast of South Korea was selected to derive detailed

251   3D winds over complex terrain (in the black box in the inset map in Fig. 1) because relatively

252   dense and high-quality wind observations were only collected in this region during ICE-POP

253   2018. The size of the WISSDOM synthesis domain is 12×12 km^2 (up to 3 km MSL height) in

254   the horizontal (vertical) direction with 50 m grid spacing. Such high spatial resolution 3D winds

255   were synthesized every 1 hour in this test. Note that the output time steps are adjustable to be

256   finer (recommended limitation is 10 mins), but they are highly related to the temporal resolution

257 of various datasets and computing resources. Two scanning Doppler lidars are located near the

258 center of the domain: one is the equipped "WINDEX-2000" (the model's name from the

259 manufacturer) at the May Hills Supersite (MHS) site, and the other is the "Stream line-XR" at

260 the DaeGwallyeong regional Weather office (DGW) site. In addition to the operational AWS

261 (727 stations), additional surface observations (32 stations) are also involved in ICE-POP 2018

262 surrounding the MHS and DGW sites and the venues of the winter Olympic Games. The

263 soundings are launched at the DGW site every 3 hours during the research period. The LDAPS

264 also provided high spatial resolution of wind information in the test domain. The horizontal

265 distribution of all instruments and datasets used are shown in Fig. 1.
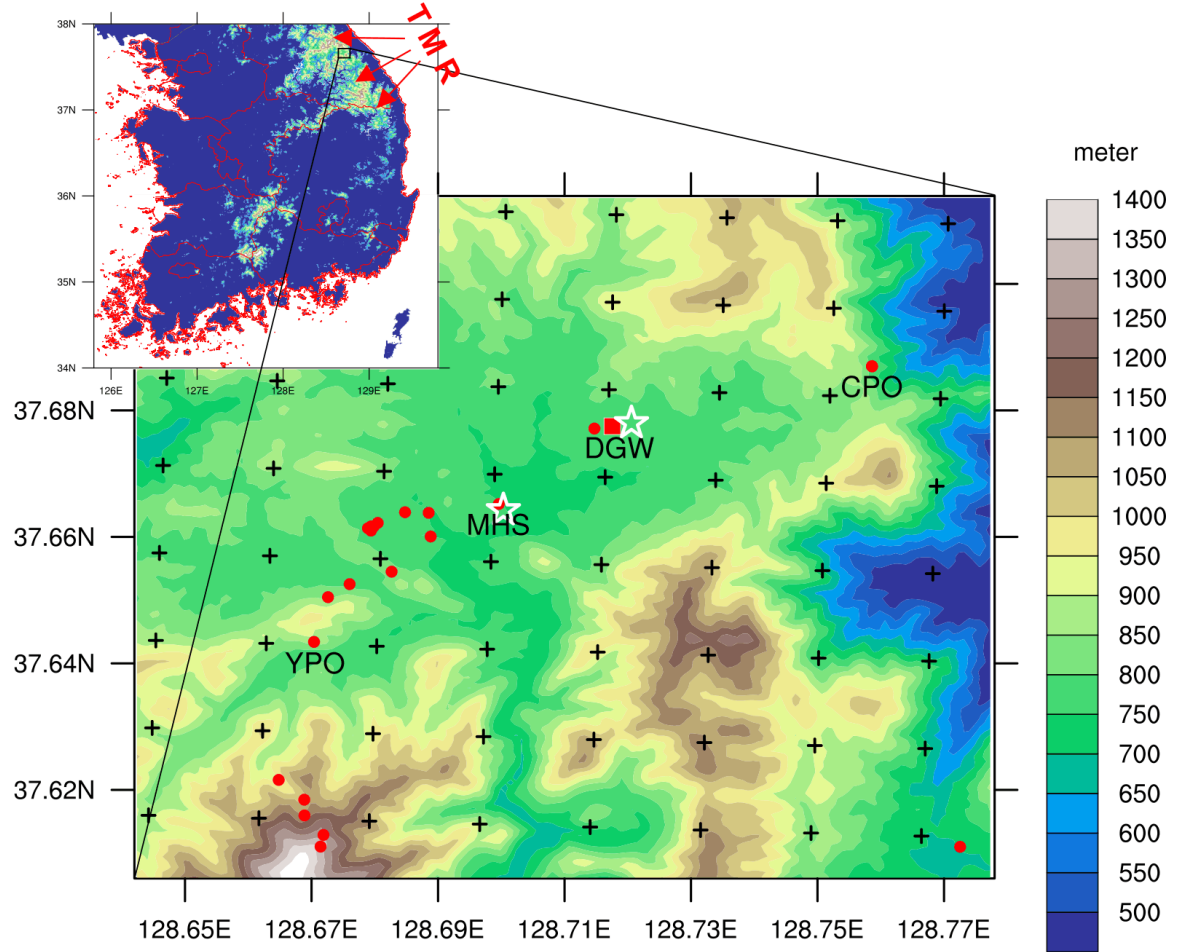
266

267 Figure 1. Horizontal distribution of instruments and datasets used in this study. A small box in the upper map

268   indicates the WISSDOM synthesis domain. The Doppler lidars are marked by start symbols at the MHS and

269   DGW sites. Red solid circles and square indicate the automatic weather station (AWS) and sounding, respectively.

270   The black cross marks the data points of LDAPS. Topographic features and elevations are shown with the color

271   shading in a color bar in the figure. The location of the Teabeak Mountain Range (TMR) is also marked.

272   **3.2 Data implemented in WISSDOM synthesis**

273   **3.2.1 Scanning Doppler lidars**

274   The radial velocity observed from two scanning Doppler lidars was utilized to retrieve 3D

275   winds via WISSDOM synthesis. The original coordinate system of observed lidar data is not a

276   Cartesian coordinate system but a spherical (or polar) coordinate system as a plan position

277   indicator (PPI) and hemispheric range height indicator (HRHI) or the RHI. Although relatively

278   dense and complete coverage of wind information (i.e., radial velocity of aerosols) were

279   sufficiently recorded by lidar observations, the collected data are usually not located directly on

280   the given grid points in the WISSDOM synthesis (i.e., Cartesian coordinate system). In this study,

281   the lidar data were interpreted simply from the lidar coordinate system to the Cartesian coordinate

282   system via bilinear interpolation.

283   The scanning strategy of the lidar at the DGW site includes five elevation angles for PPI (7°,

284   15°, 30°, 45°, and 80° before 10:00 UTC on 14 Feb. 2018 and 4°, 8°, 14°, 25°, and 80° after 10:00

285   UTC) and two HRHIs at azimuth angles of 51° and 330°. A full volume scan included all PPIs

286   and HRHIs every ~12 min. The maximum observed radius distance is ~13 km, and the grid

287   spacing is 40 m for each gate along the lidar beam. The scanning strategy of the lidar at the MHS

288   site involves seven elevation angles for PPI (5°, 7°, 10°, 15°, 30°, 45°, and 80°) and one HRHI

289   at an azimuth angle of 0°. A full volume scan included all PPIs and RHIs every ~12 min. The

290   maximum observed radius distance was ~8 km, and the grid spacing was 60 m. The vertical

291   distribution of lidar data in the test domain is shown as blue lines in Fig. 2a.

292   **3.2.2 Automatic weather station (AWS)**

293   Most of the AWS are not exactly located on the given grid points of the Cartesian coordinate

294   system. Objective analysis (Cressman, 1959) is a popular way to correct semirandom and

295   inhomogeneous meteorological fields into regular grid points. Notably, that the wind directions

296   and speed must be the first project with the values along the u- and v-components, and then,

297   their values must be interpolated individually to the given grids. This study adopted objective

298   analysis for the AWS observations with adjustable RI distances between 100 m and 2000 m. After

299   this first step, the observational data can reasonably interpolate to the given grid points

300   horizontally. Furthermore, an additional step is required to put these interpolated data into the

301   given grid points at different vertical levels because the AWS are located at different elevations

302   in the test domain. In the traditional way of original WISSDOM, the interpolated data are moved

303   to the closest level with the shortest distance just above the AWS site. However, the interpolated

304   data are NOT moved to the closest level if the shortest distances are large like more than half

305   (50%) of grid spacing. Nevertheless, to include more data from the AWS observations

306   appropriately, adjusted distances between the AWS sites and given grid points at different vertical

307   levels were necessarily considered. These adjusted distances can be named as vertical extension

308   (VE) here, and there are two options of 50% and 90% in the tests of this study, which correspond

309   to 25 m and 45 m extensions between each grid (in case of the grid spacing is 50 m), respectively.

310   An example demonstrated how to implement the interpolated data to the given grid points by

311   adjustable VE after step one (Fig. 2b).

312   In Fig. 2b, the interpolated data do not need to move to a given grid point (as an example, at

313   the 800 m level here) if the elevation of the AWS is equal to the height of a given grid point as

314   point A. When the AWS is located higher than a given grid point (as point B in Fig. 2b) and does

315   not reach the lower boundary of VE (50%) from the upper given grid point (i.e., at the 850 m

316   level), this interpolated data will be removed and wasted. In contrast, when the interpolated data

317   are located just below the given grid point with 50% VE, it will be achieved in the WISSDOM

318   synthesis at the 800 m level (point C in Fig. 2b). The interpolated data of point D have a similar

319   situation to point B; however, it will be achieved at the 800 m level because a higher VE (90%)

320   was applied here. Since the locations of the AWS are semirandom with relatively sparse or

321   concentrated distributions, the optimal RI and adjustable VE make it possible to include more

322   AWS observations in the WISSDOM synthesis.
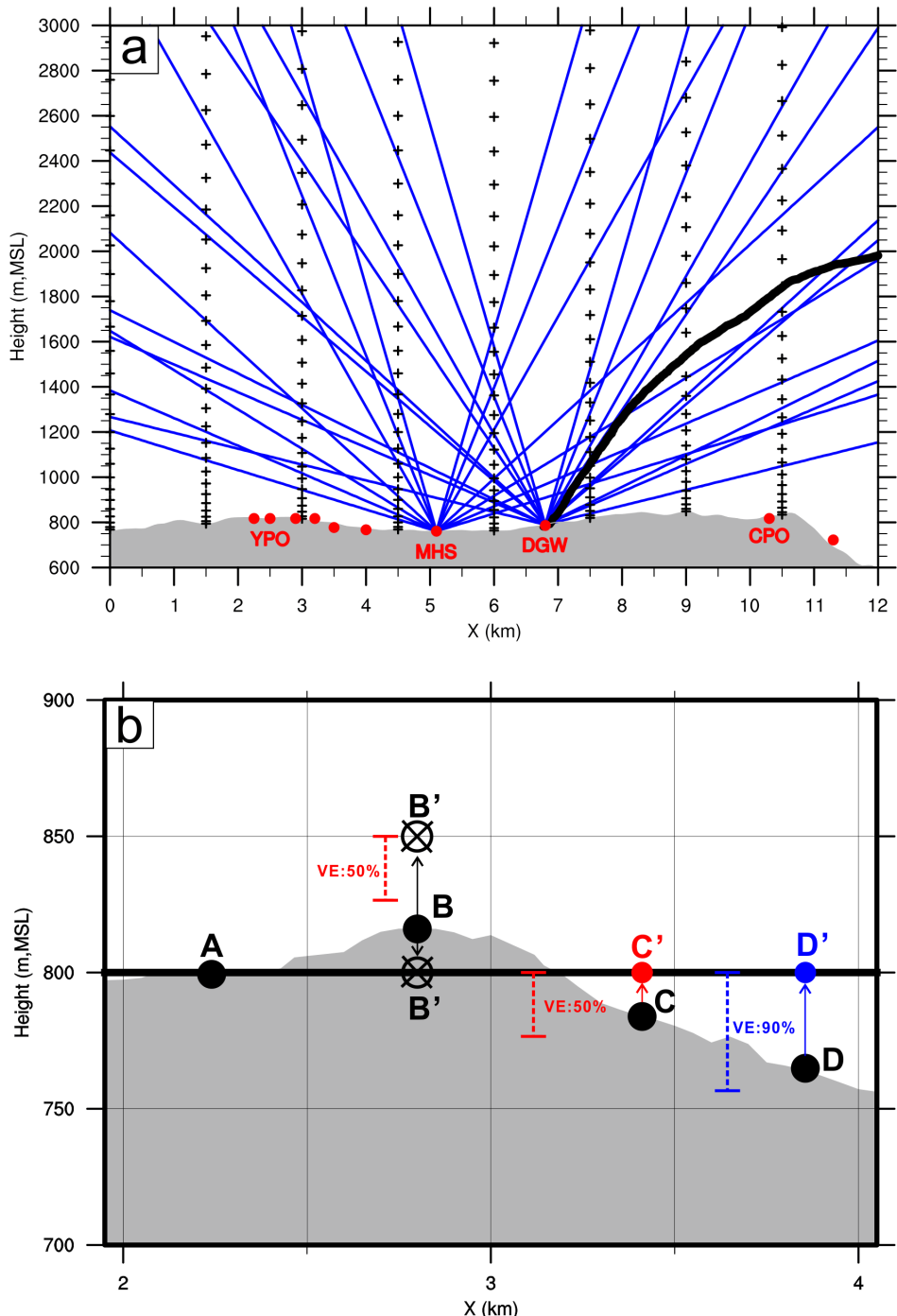
323
324   Figure 2. (a) Schematic diagram of the vertical distribution of adopted lidar datasets. Blue lines indicate the lidar
325   data observed at the DGW and MHS sites with different elevation angles. The AWS are located on the ground
326   and are marked by solid red circles. An example of a sounding track launched from the DGW site in one time
327   step (06:00 UTC on 14 Feb. 2018) is plotted as a thick black line. The black cross marks indicate the vertical
328   distribution of the LDAPS dataset. (b) Schematic diagram for data implementation with various locations of the
329   AWS and different percentages of VE (vertical extension) from given grid points at the 800 m MSL level (thick
330   black line). The gray shading on the bottom represents the topography.

3.2.3 Sounding

During ICE-POP 2018, the soundings are launched at the DGW site every 3 hours (from 00Z). Vertical profiles of air pressure, temperature, humidity, wind speed and directions were recorded every second (i.e., ~3 m vertical spatial resolution) associated with the rising sensor. The sounding sensor drifted when rising, and an example of its track in one time step is shown as a thick black line in Fig. 2a. In this example, the sounding movement was mostly affected by westerly winds, and it measured the meteorological parameters in any location along the track in the test domain. The coordinate system of sounding data is quite similar to the distribution of AWS measurements, and the observations are not located right on the given grid points of the WISSDOM synthesis.

Similar to the AWS data, the sounding data also underwent objective analysis with an adjustable RI distance for the wind measurements in the first step. Then, the interpolated data were switched to given grid points for each vertical level by the different VE in the WISSDOM synthesis.

3.2.4 Reanalysis dataset: LDAPS

The local reanalysis dataset LDAPS was generated by the KMA. This dataset provides u- and v-component winds every 3 hours, and the horizontal spatial resolution is ~1.5 km with the grid type in Lambert Conformal (as black cross marks in Fig. 1). The data revealed denser distributions near the surface and sparse distributions at higher levels (see Fig. 2a). The initiations of wind variables in the LDAPS were assimilated with many observational platforms, including radar, AWS, satellite and sounding data. Thus, the relatively high reliability of this dataset could be expected. In addition, such datasets have also significantly improved the forecast ability in small-scale weather phenomena over complex terrain in Korea (Kim et al., 2019, Choi et al., 2020, Kim et al., 2020).

355   The LDAPS data are not located directly on the given grid points of the WISSDOM synthesis

356   system. Unlike the distribution of AWS and sounding observations, LDAPS has dense and good

357   coverage in the test domain. The Cartesian coordinate is the most efficient method and the best

358   system for partial differential equations (Armijo, 1969), and it is also used in the cost function of

359   WISSDOM (Liou and Chang, 2009). In this study, the horizontal and vertical resolutions of given

360   grid points were primarily determined by the characteristics of lidar data. Therefore, similar to

361   lidar observations, the LDAPS data were also interpolated to the given grid points on the

362   Cartesian coordinate system via the bilinear interpolation method.

363   **3.3 Overview of the selected strong wind event**

364   A strong wind event was selected to evaluate the performance of this modified WISSDOM

365   synthesis scheme. In this strong wind event, the evolution of surface wind patterns on the Korean

366   Peninsula was mainly dominated by a moving LPS which is one type of strong downslope winds

367   (Park et al, 2022, Tsai et al., 2022). The LPS moved out from China and penetrated the northern

368   part of the Korean Peninsula through the Yellow Sea beginning at approximately 12:00 UTC on

369   13 February 2018. Consequently, a relatively strong surface wind speed (exceeding ~17 m s^{-1})

370   was observed when the LPS was located near the northeastern coast of the Korean Peninsula

371   (~130°E, 40°N) at 00:00 UTC on 14 February 2018 (Fig. 3). Then, the surface wind speed became

372   weak when the LPS moved away from South Korea after 00:00 UTC on 15 February 2018 (not

373   shown); the details of the synoptic conditions can be found in Tsai et al. (2022).
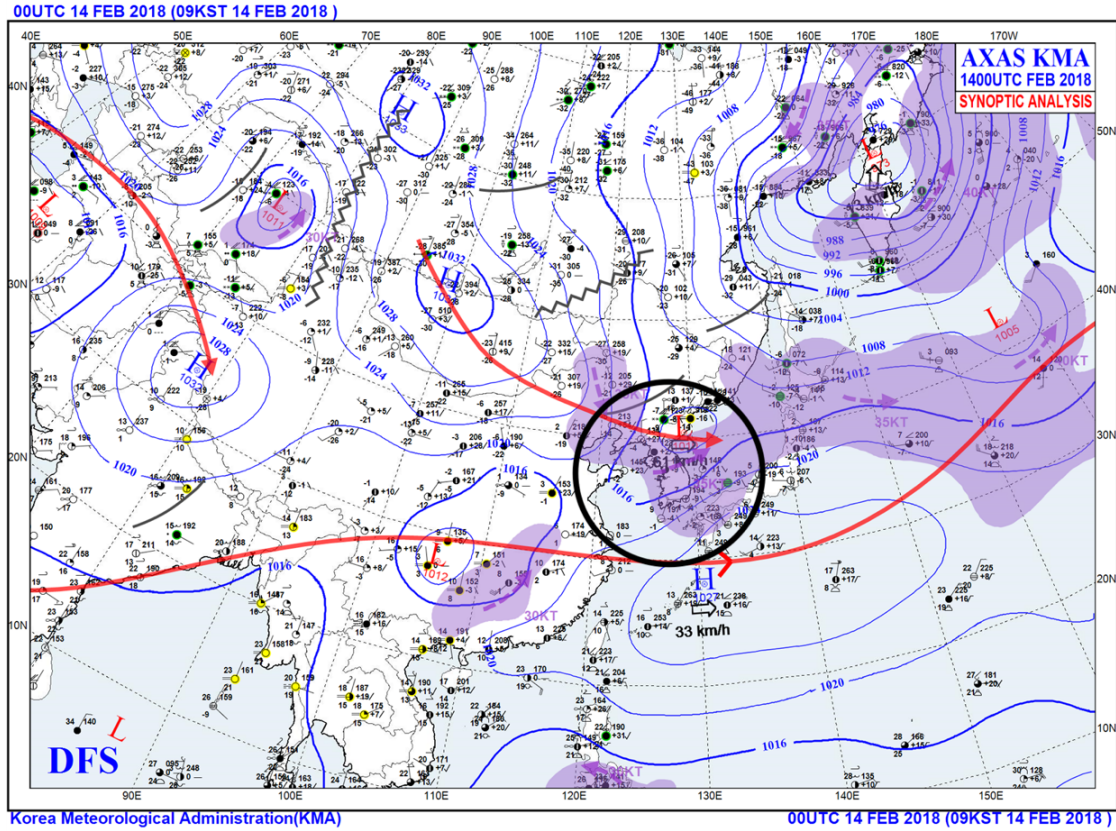
Figure 3. Synoptic surface chart from the Korea Meteorological Administration (KMA) at 00:00 UTC on 14 Feb. 2018. The locations of the Korean peninsula and the LPS has been marked by black circle.

This event is one of two strong wind events (i.e., daily maximum wind speeds larger than 10 m s^{-1} observed at the AWS sites along the northeastern coast of South Korea) in the past decade based on the KMA historic record. Such a strong wind event may help us to examine the potential maximum errors of the retrieved winds. Since persistent, strong westerly winds were observed by the soundings and AWS from near the surface and upper layers over the TMR during the event, the data coverages in the test domain were checked during a chosen time step (06:00 UTC on 14 February 2018). The percentage of data occupations for each dataset (after interpolation) was checked, and the results are shown in Fig. 4. Note that the elevation of the TMR is approximately 700 m MSL in the test domain. The lidars provided good coverage of 100% to 50% at the lower layers between 700 m and 800 m MSL. The coverage of lidars was reduced significantly above 900 m MSL and remained at ~5% due to the scan strategy during the Olympic games (more dense observations near the surface). The maximum coverage of the AWS

390 observations is ~40% at 800 m, and there was less coverage above this layer since relatively few

391 AWS are located in the higher mountains. Because only one sounding observation was utilized

392 in this domain, relatively few coverages were also depicted. The local reanalysis LDAPS can

393 provide complete coverage above 900 m MSL (exceeding 100%), albeit there was less coverage

394 in the lower layers due to terrain. The lidar, sounding, and AWS observations covered most areas

395 at lower levels but not higher levels; thus, the LDAPS compensated for most of the wind

396 information at the upper layers in the WISSDOM synthesis.
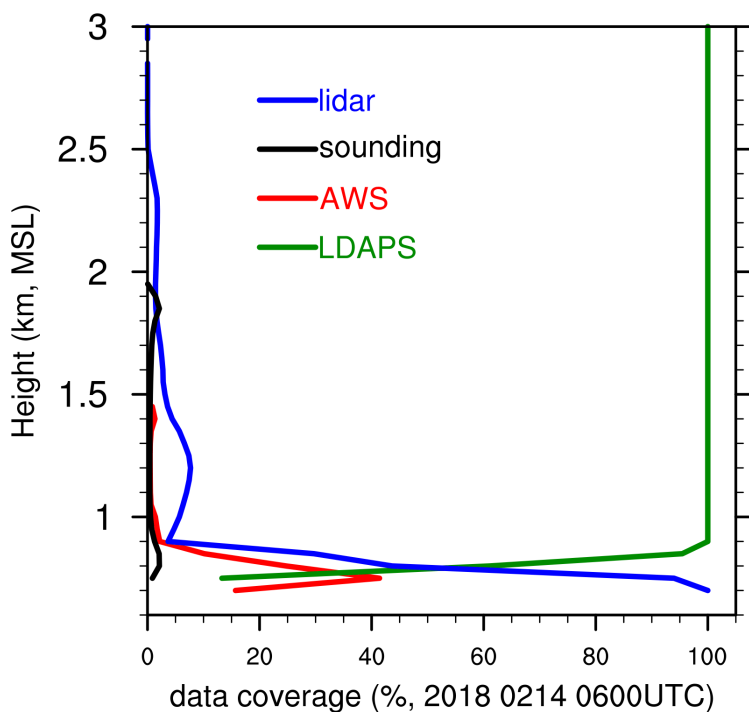
397

398 Figure 4. Data coverage (percentage, %) of the lidar (blue line), sounding (black line), AWS (red line) observations,

399   and LDAPS (green line) at 06:00 UTC on 14 Feb. 2018.

4. Control run and the accuracy of WISSDOM

4.1 Control run

402   Relatively reliable 3D winds were derived by a control run of the WISSDOM synthesis

403 because all available wind observations and local reanalysis datasets were appropriately acquired.

404 These datasets provided sufficient and complete wind information with a high percentage of

405 coverage in the test domain (cf. Fig. 4). Therefore, the retrieved winds from the control run can

406 be treated as the optimal results in WISSDOM. The control run was performed carefully with the

407 necessary procedures in data implementation before running the WISSDOM synthesis as follows.

408 The lidar and LDAPS datasets must perform bilinear interpolation to the given grid points in

409 WISSDOM, and the sounding and AWS observations must undergo objective analysis with the

410 appropriate RI distance and VE. The quantities of the weighting coefficients for each input dataset

411 followed the default setting from the original version of WISSDOM. The 3D winds were derived

412 during one time step at 06:00 UTC on 14 Feb. 2018 and compared with conventional

413 observations. Note that the best weighting coefficients have been determined by a series of

414 observation system simulation experiment (OSSE) type tests from Liou and Chang (2009). They

415 put more weighting coefficients in observations and fewer in modeling inputs. Based on the

416 experiences and the default setting of weighting coefficients from their studies, the basic setting

417 of the control run was first decided. Consequently, sensitivity tests were performed to better

418 understand the possible variances associated with different weighting coefficients when the lidar

419 data were implemented. The basic setting of this control run is summarized in Table 1.

Table 1   Basic setting of WISSDOM (control run)

Domain Range	Latitude: 37.606°N~37.713°N Longitude: 128.642°E~128.778°E
Domain Size	12 × 12 × 3 km (long × width × vertical)
Spatial Resolution	0.05 × 0.05 × 0.05 km (long × width × vertical)
Terrain Resolution	0.09 km
Coordinate System	Cartesian coordinate system
Background	Sounding (DGW)
Data Implementation	Doppler Lidars (MHS, DGW): bilinear interpolation AWS: objective analysis (RI*: 1 km, VE*: 90%) Sounding (DGW): objective analysis (RI: 1 km, VE: 90%) LDAPS: bilinear interpolation
Weighting Coefficient (input datasets)	Doppler Lidars (α_1): 10^6 Background (α_2):10^2

Sounding (α_6): 10^6	
AWS (α_7): 10^6	
LDAPS (α_8): 10^3	

*RI: radius influence, VE: vertical extension

420   The results of 3D winds at 800 m MSL derived from the control run are shown in Figs. 5a,

421   c, and e. Topographic features comprised relatively lower elevations in the center of the test

422   domain, and there were weaker u-component winds (~7 m s^{-1}) near the AWS and MHS lidar sites

423   between 128.67°E and 128.71°E (Fig. 5a). In contrast, the u-component winds (~15 m s^{-1}) were

424   almost doubled near the DGW lidar site (between 128.71°E and 128.73°E). The vertical

425   structures of the u-component winds across these two lidars (i.e., along the black line in Fig. 5a)

426   are shown in Fig. 5b. The strength of the u-component winds rapidly increased from the surface

427   to the upper layers (from ~6 to 20 m s^{-1}), and uniform u-component winds with wavy pattern

428   were depicted above ~1 km MSL except for the stronger winds near the surface surrounding the

429   DGW site. There were relatively weak (strong) u-component winds surrounding the lidar at the

430   MHS (DGW) site near the surface. Relatively weak v-component winds were found

431   (approximately ±4 m s^{-1}) at 800 m MSL (Fig. 5c); thus, the horizontal wind directions were

432   mostly westerly winds during this time step. The v-component winds were obviously accelerated

433   in several local areas encompassing the terrain (near 128.71°E). The vertical structure of the v-

434   component winds (Fig. 5d) indicates that the v-component winds became stronger in the upper

435   layer. The wind directions were changed from westerly to southwesterly from the near surface

436   up to ~1.4 km MSL height. Updrafts were triggered on windward slopes when westerly winds

437   impinge the terrain or hills (Figs. 5e and 5f). Basically, the 3D winds derived from the WISSDOM

438   synthesis reveal reasonable patterns compared to synoptic environmental conditions (cf. Fig. 3);

439   the moving LPS accompanied stronger westerly winds.

440
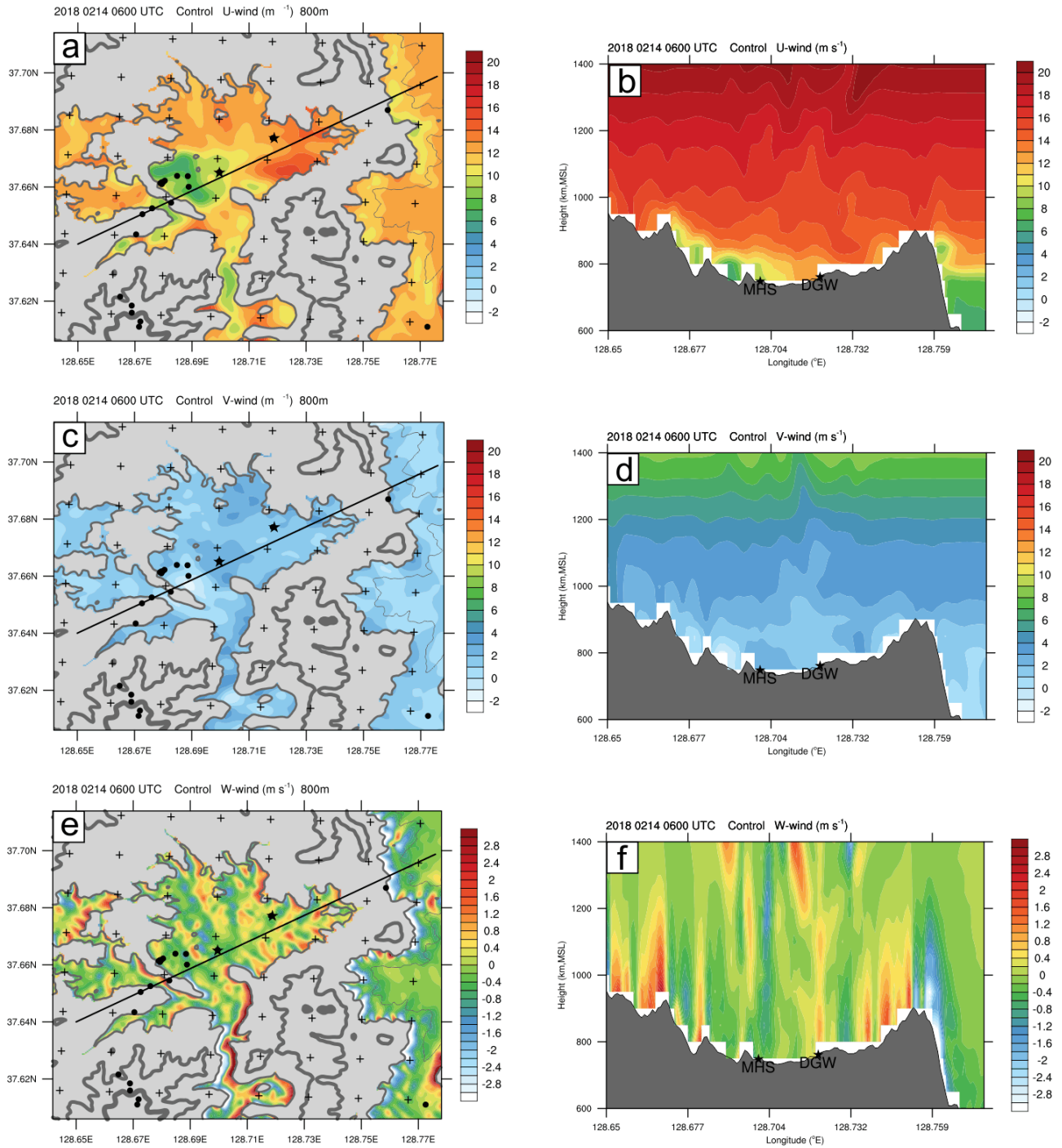
Figure 5. The 3D winds were derived from the control run by the WISSDOM synthesis at 06:00 UTC on 14 Feb.
2018. (a) The u-component winds (color, m s⁻¹) at 800 m MSL; the gray shading represents the terrain area, and
the contours indicate different terrain heights of 600 m, 800 m and 1000 m MSL corresponding to thin to thick
contours. The locations of lidars are marked with asterisks. (b) Vertical structures of u-component winds (color,
m s⁻¹) along the black line in (a) The gray shading in the lower part of the figure indicates the height of the terrain.
(c) and (d) are the same as (a) and (b) but for the v-component winds. (e) and (f) are the same as (a) and (b) but
for the w-component winds.

4.2 Intercomparison between derived winds and observations

Detailed analyses were performed in this section to quantitatively evaluate the accuracy of the optimally derived 3D winds from the WISSDOM synthesis. Two kinds of instruments were available in the test domain to detect the relatively realistic winds: sounding and lidar quasi-vertical profiles (QVP, Ryzhkov et al., 2016). The QVP of horizontal and vertical winds were retrieved based on the so-called velocity-azimuth display (VAD) technique (Browning and Wexler, 1968, Gao et al., 2004). We regressed the Fourier coefficients of the Doppler velocities of the 80° PPI under the linear horizontal wind assumption and obtained the horizontal wind profile. The vertical (i.e., w-component) wind was retrieved under the assumptions of constant vertical wind, zero terminal velocity of aerosol particles, and no horizontal divergence [see Kim et al. (2022) for details on the wind retrieval]. The accuracy of the retrieved wind profile is suitable for the WISSDOM wind evaluation, given the low root mean square deviation (RMSD) of < 2.5 m s^{-1} and high correlation coefficient of > 0.94 of horizontal wind speed as shown in the comparison against 487 rawinsondes (Kim et al., 2022). The horizontal winds observed from the soundings and the u-, v-, and w-component winds of the lidar QVP at the DGW site were utilized to represent the observations.

A complete analysis of the intercomparison between the WISSDOM synthesis and observations is presented in the following subsections. Because the verification observations are being used in the WISSDOM synthesis, the results of the control run are not verified independently; nevertheless, detailed discussions regarding the results of the sensitivity tests for the observations are presented in Section 5.

4.2.1 Sounding

The discrepancies in horizontal winds derived from WISSDOM and the sounding observations for the entire research period (from 12:00 UTC on 13 to 12:00 UTC on 14 February

472   2018) were analyzed. Fig. 6 shows the scatter plots of the u- and v-component winds on the

473   locations following the tracks of sounding launched from the DGW site. Most of the u-component

474   winds derived from WISSDOM are in good agreement with the sounding observations, and the

475   wind speed is increased with the height from approximately 10 to 40 m s^{-1}. Slight underestimation

476   of retrieved u-component winds can be found at the layers of 1.5~2 km MSL (Fig. 6a). In contrast,

477   most of the v-component winds were weak (smaller than 15 m s^{-1}) at all layers, because the

478   environmental winds were more like westerlies during the research period. There were also

479   slightly overestimated v-component winds derived from WISSDOM at the layers of 1.5~2 km

480   MSL (Fig. 6b). The possible reason why the overestimated winds occurred above ~1.5 km MSL

481   is that lidar data had relatively less coverages at higher layers (cf. Fig. 4).
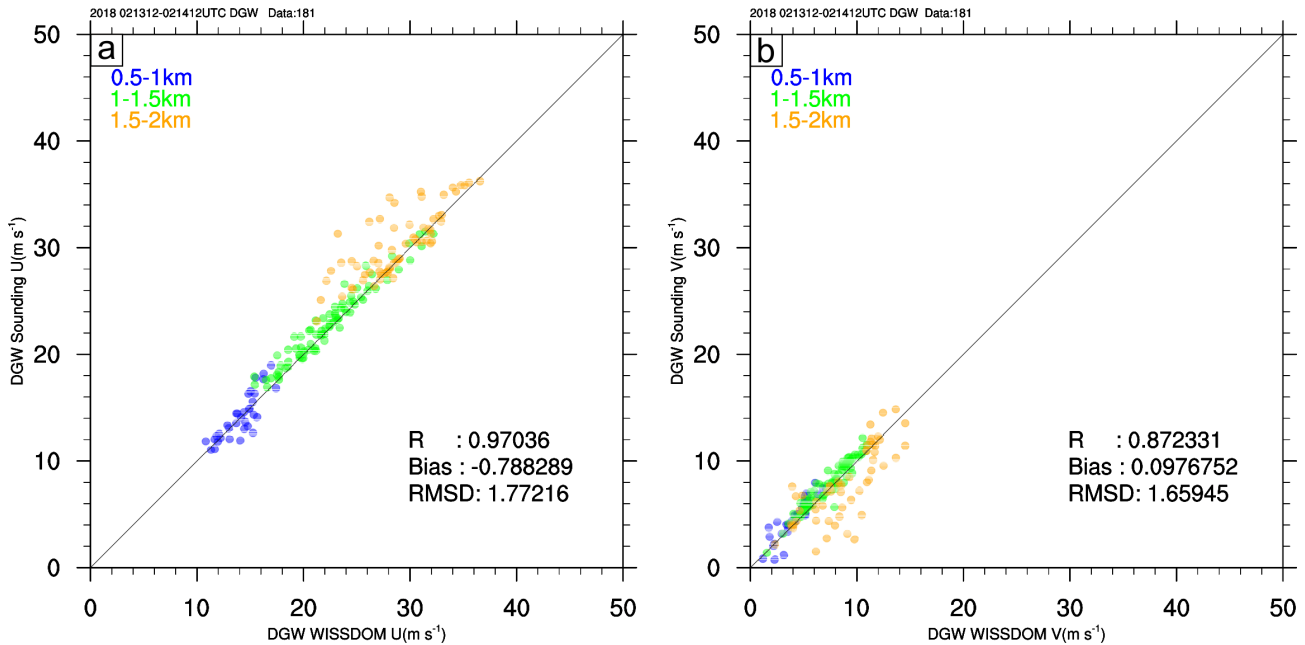
483   Figure. 6. Scatter plots of (a) u-component winds between the WISSDOM synthesis (x-axis) and sounding
484   observations (y-axis) above the DGW site during the research period. The colors indicate different layers, and
485   the numbers of data points, correlation coefficients, average biases and root mean square deviations are also
486   shown in the figure. (b) The same as (a) but for v-component winds.

487   Overall, the u-component winds show a high correlation coefficient (exceeding 0.97), low

488   average bias (−0.78 m s^{-1}), and the RMSD of 1.77 m s^{-1}. The correlation coefficient of the v-

489   component is also high (0.87), the average bias is 0.09 m s^{-1}, and the RMSD is 1.65 m s^{-1}.
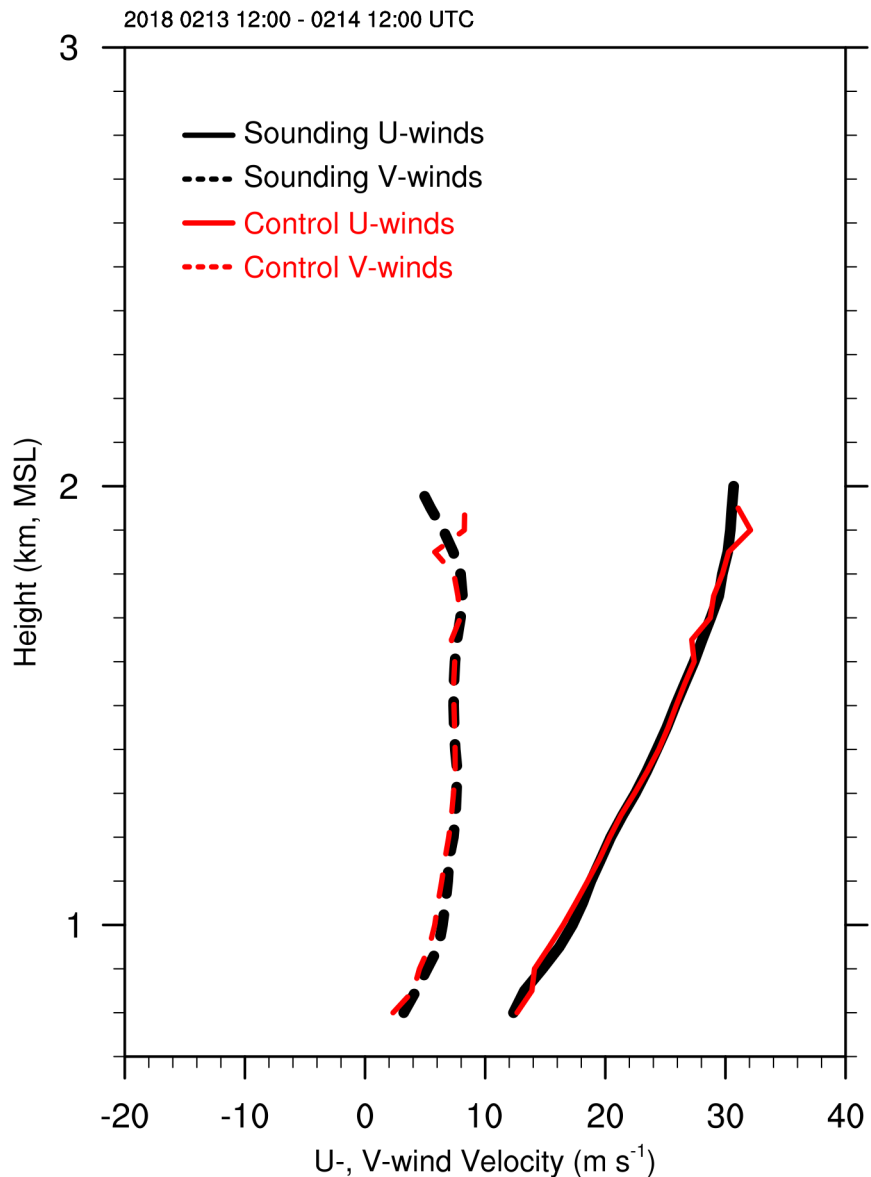
490

491 Figure 7. Vertical wind profiles of average horizontal winds derived from the WISSDOM synthesis (red lines and

492  vectors) and sounding observations (black lines and vectors) above the DGW site from 12:00 UTC on 13 to

493  12:00 UTC on 14 Feb. 2018. Solid lines indicate u-component winds (m s^{-1}), and dashed lines indicate v-

494  component winds (m s^{-1}).

495   The vertical profiles of the averaged u- and v-component winds for the period of 12:00 UTC

496 on 13 to 12:00 UTC on 14 Feb. 2018 is shown in Fig. 7 for the WISSDOM synthesis (red) and

497 sounding observations (black) launched from the DGW site. The average profiles agree well

498 except for the height above 1.5 km MSL, slight discrepancies of u- and v-component winds (< 1

499 m s^{-1}). Their statistical errors during the entire research period were quantified by the box plot

500 shown in Fig. 8.

501   The maximum difference in wind directions between the WISSDOM synthesis and sounding

502   observations is small at all layers. Only relatively larger IQR (between ~−5 and 5 degrees) and

503   larger median values (between ~0 and 5) can be found at the lowest level. The interquartile range

504   (IQR) and median values of the wind direction differences are smaller (between ~0 and 2.5

505   degrees) during the entire research period (Fig. 8a). Basically, the IQR and median values of the

506   wind direction differences are close to 0 degrees above 1 km MSL. Fig. 8b shows the difference

507   in wind speed between the WISSDOM synthesis and sounding observations. The differences of

508   wind speed derived from WISSDOM was slightly underestimated in the layers between ~0.85

509   and 1.3 km MSL. The median values of the wind speed differences were between −1 and 0.5 m

510   s^{-1}, and the IQR of wind speed differences was between −2 and 0.5 m s^{-1}. Above 1.3 km MSL,

511   the differences in wind speed are small as their median values are close to 0 m s^{-1}.

512
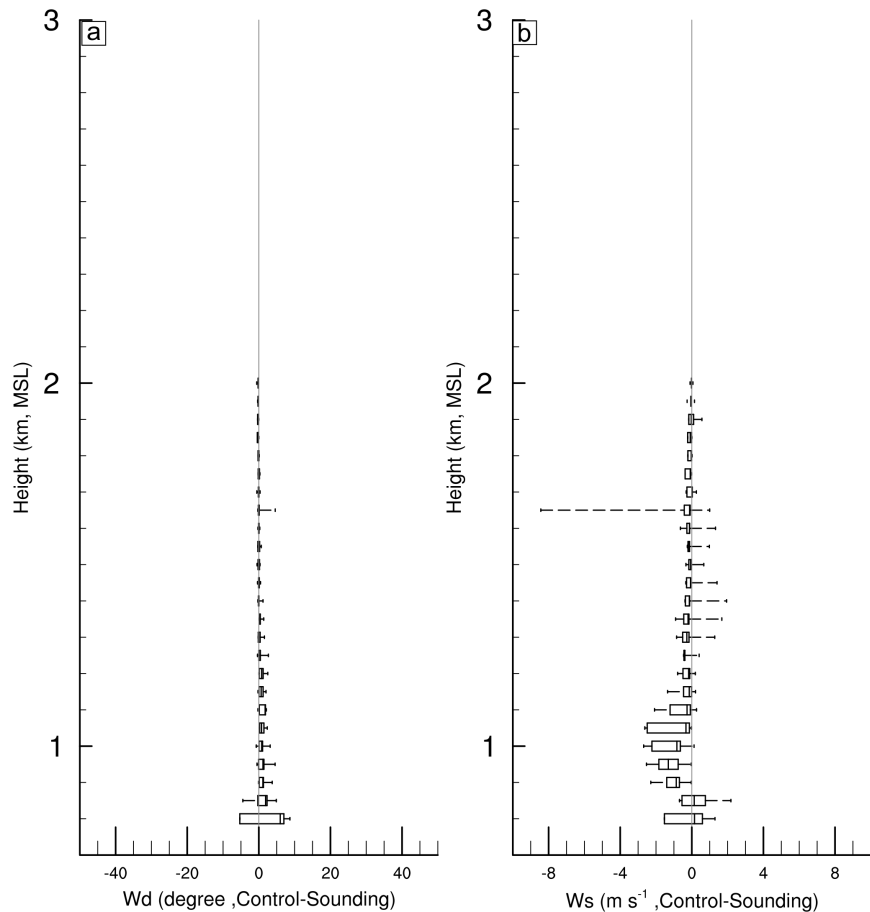
513

514   Figure 8. The box plot of average (a) wind direction discrepancies between the WISSDOM synthesis and sounding

515   observations above the DGW site during the research period. (b) Same as (a) but for the wind speed.

4.2.3 Lidar QVP

The lidar QVP is another observational reference used to evaluate the performance of derived winds from the WISSDOM synthesis. The scatter plots of the horizontal winds derived from WISSDOM and lidar QVP at the DGW site are shown in Fig. 9. The strength of the u-component winds increases with height in the range between approximately 10 m s^{-1} and 40 m s^{-1} from the surface up to ~2.5 km MSL (Fig. 9a). Although the results show a relatively high correlation coefficient (0.84) for the u-component winds from lower to higher layers in the entire research period, the degree of scatter is larger than that in Fig. 6a. The average bias and RMSD of the u-component winds are 2.83 m s^{-1} and 3.69 m s^{-1}, respectively. The correlation coefficient of v-component winds is lower (0.35) in association with low wind speed (<15 m s^{-1}) from the surface to 2.5 km MSL (Fig. 9b), and it may possibly relate to less coverage from lidar QVP data at higher layers. The average bias and RMSD of the v-component winds are 2.26 m s^{-1} and 2.92 m s^{-1}, respectively. The results of these scatter plot analyses are summarized in Table 2. Basically, the u-component winds have high correlations, relatively lower bias, and lower RMSD than the v-component winds because the environmental winds are more westerly.
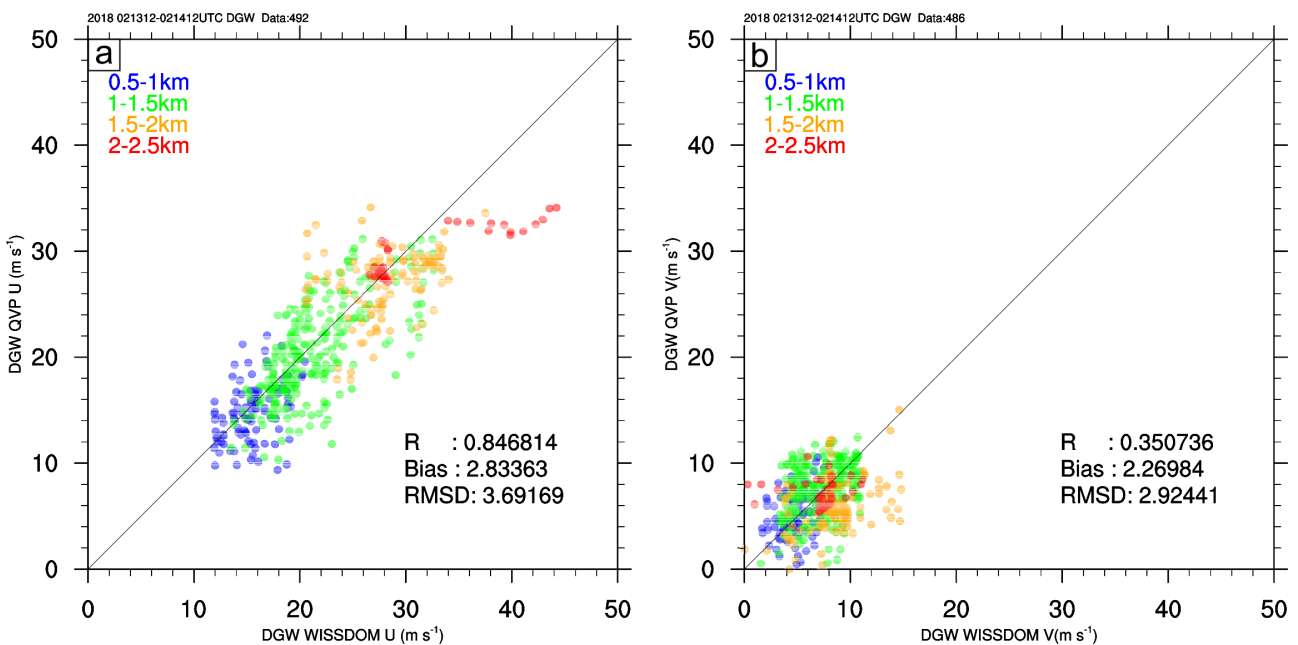
Figure 9. The same as Fig. 6 but for (a) u-component winds between the WISSDOM synthesis (x-axis) and lidar QVP (y-axis). (b) The same as (a) but for v-component winds.

534

Table 2 Summary of the intercomparisons between WISSDOM and observations

		Correlation coefficient	Average bias (m s^{-1})	RMSD (m s^{-1})
WISSDOM-sounding	u-component	0.97	-0.78	1.77
	v-component	0.87	0.09	1.65
WISSDOM-lidar QVP	u-component	0.84	2.83	3.69
	v-component	0.35	2.26	2.92

535   Compared to the sounding observations, additional w-component winds are available in

536   lidar QVP, which allows us to check their discrepancies in 3D winds. However, most of the

537   vertical velocity observations were quite weak (approximately ±0.2 m s^{-1}) above the DGW site,

538   and relatively low reliability of the derived vertical velocity could be expected in this event.

539   Therefore, the average vertical profiles of 3D winds were utilized to qualitatively check the

540   discrepancies between WISSDOM synthesis and lidar QVP during the research period (Fig. 10).

541   The results show that the average u-component winds have relatively smaller discrepancies

542   (approximately <1 m s^{-1}) between the WISSDOM synthesis (marked as WISS-U in Fig. 10) and

543   lidar QVP (marked as QVP-U) below ~1.3 km MSL at the DGW site. In contrast, there were

544   larger discrepancies (approximately >2 m s^{-1}) between 1.3 km and 2 km MSL. The average v-

545   component winds derived from WISSDOM (marked as WISS-V) and lidar QVP (QVP-V) were

546   generally weak, and the ranges of WISS-V and QVP-V were between ~2 m s^{-1} and 8 m s^{-1}.

547   Generally, the vertical profiles of WISS-V were nearly overlain with QVP-V, and their

548   discrepancies existed in the height range 1.6~2.0 km MSL (maximum ~4 m s^{-1}). Smaller (larger)

549   discrepancies of w-component winds were significantly below (above) the height at ~1.3 km

550   MSL (maximum discrepancies ~0.6 m s^{-1} at 1.7 km MSL). Despite the larger discrepancies, the

551   similar patterns of W can also be shown. In summary, the discrepancies in the 3D winds between

552   the WISSDOM synthesis and lidar QVP were small in the lower layers and large in the higher

553   layers because the observational data from lidars and AWS provided good quality and sufficient

554   wind information at the lower layers but not in the higher layers (lower coverages of lidar data

555 above 1.3 km MSL, cf. Fig. 4).
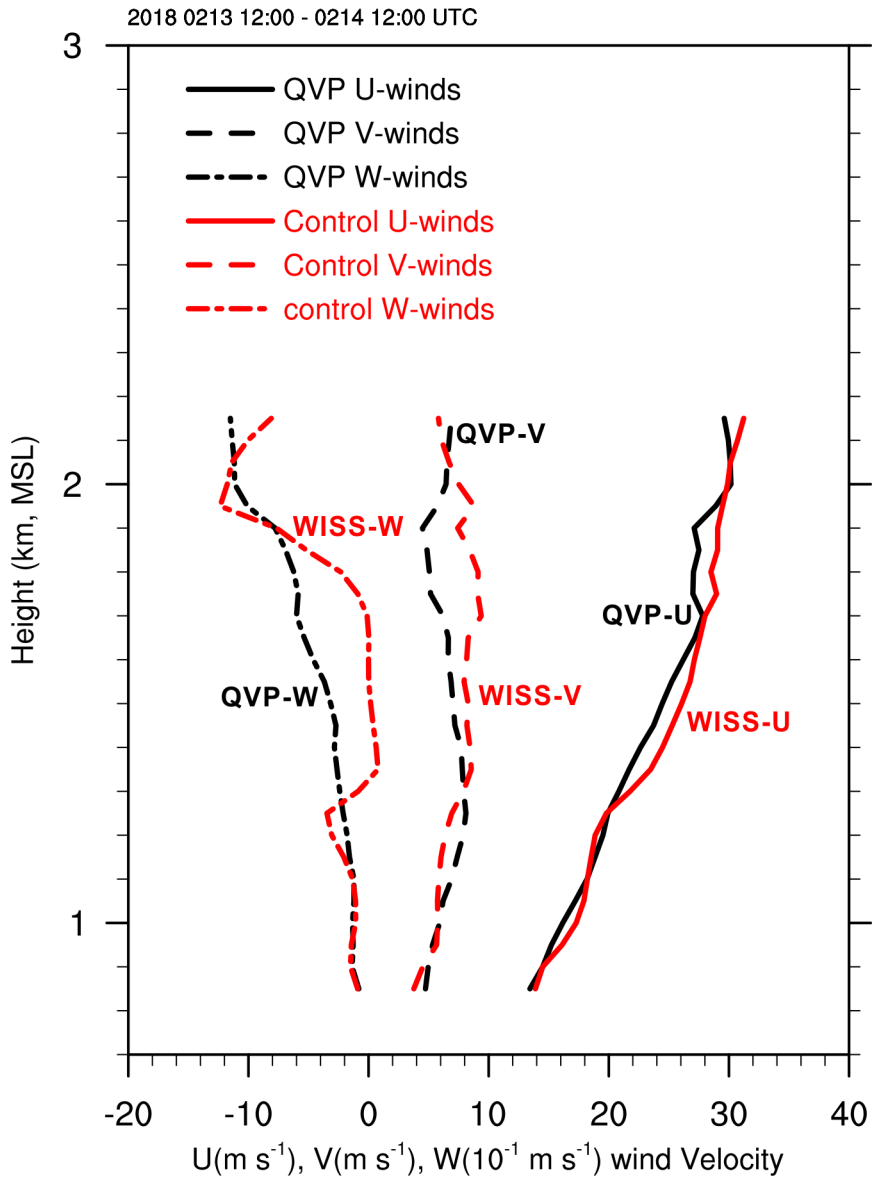
Figure 10. Vertical wind profiles of average 3D winds derived from the WISSDOM synthesis (red lines and vectors)
  and lidar QVP (black lines and vectors) above the DGW site from 12:00 UTC on 13 to 12:00 UTC on 14 Feb.
  2018. Solid lines indicate u-component winds (m s^{-1}), dashed lines indicate v-component winds (m s^{-1}), and
  dash-dotted lines indicate w-component winds (1×10^1 m s^{-1}). The u-, v-, and w-component winds derived from
  the WISSDOM synthesis (lidar QVP) were marked by WISS-U (QVP-U), WISS-V (QVP-V), and WISS-W
  (QVP-W), respectively.

563   Fig. 11 shows the quantile distribution of statistical errors of wind direction, wind speed and

564 vertical velocity between the WISSDOM synthesis and lidar QVP during the research period.

565 The IQR of the wind direction is smaller (−5~5 degrees) in the layers from 0.85 km to 1.5 km

566 MSL and turns to approximately −10~0 degrees above 1.5 km MSL. The median values of wind

567 direction are smaller −5~5 degrees) from near the surface to the upper layers (Fig. 11a). Fig. 11b

568 shows that the median values (IQR) of wind speed are approximately –1~1 m s^{-1} (–2~2 m s^{-1})

569 below 1.5 km MSL, and they all become larger with heights above 1.5 km MSL (between −1 and

570 3 m s^{-1} for median values and −4~4 m s^{-1} for the IQR). The statistical error of the vertical velocity

571 reveals that the IQR is −0.2~0.2 m s^{-1} (−0.8~0.8 m s^{-1}) below (above) 1.3 km MSL, and the

572 median values are 0~0.2 m s^{-1} −0.2~0.6 m s^{-1}) below (above) 1.3 km MSL. The results of

573 statistical errors are summarized in Table 3.

574
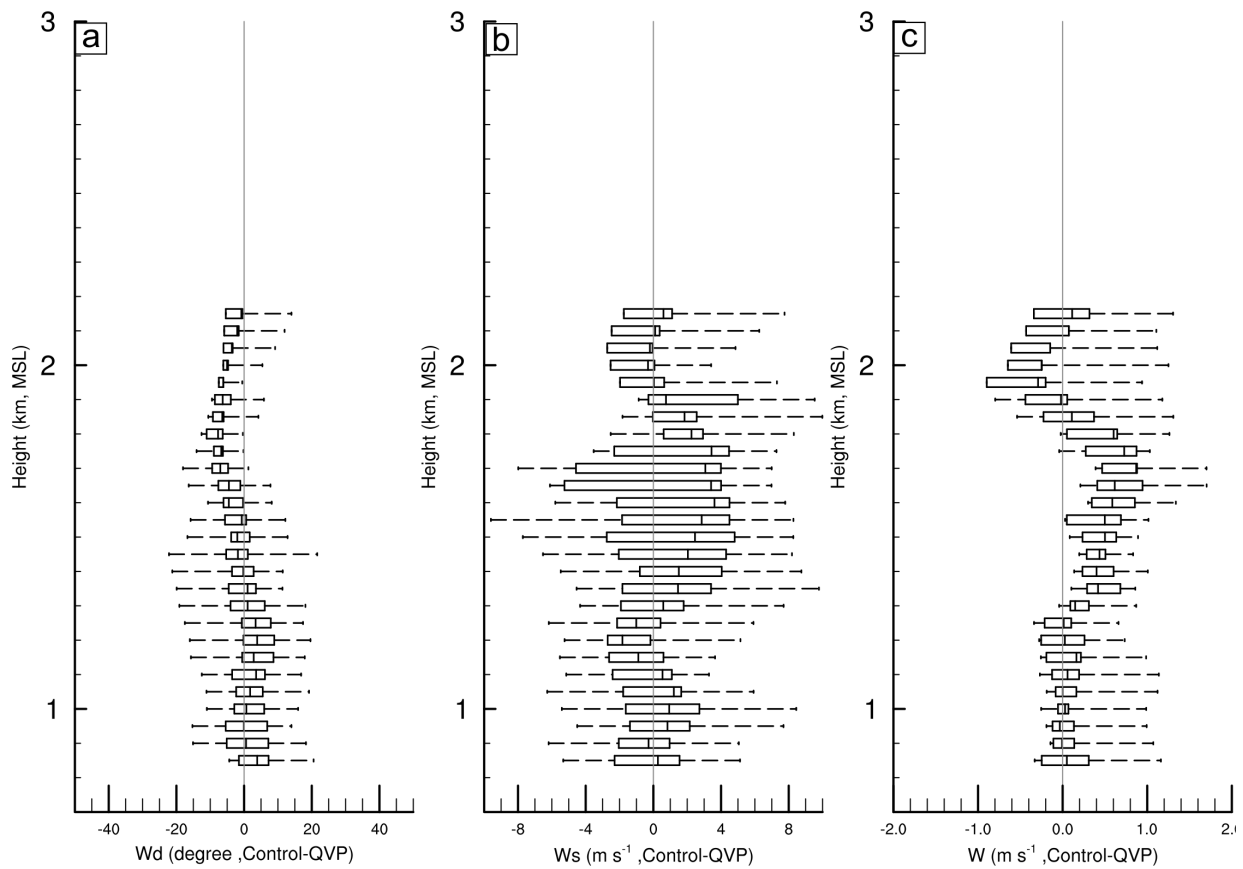
575

576 Figure 11. The box plot of average (a) wind direction discrepancies between the WISSDOM synthesis and sounding

577 observations above the DGW site during the research period. (b) Same as (a) but for the wind speed. (c) Same

578 as (a) but for the w-component winds.

579

Table 3 Summary of the statistical errors between WISSDOM and observations

		Interquartile range (IQR)	Median values
WISSDOM-sounding	wind direction	0~2.5 (deg.)	0~2.5 (deg.)

	wind speed	−2~0.5 (m s^{-1})	−1~0.5 (m s^{-1})
	wind direction	−10~5 (deg.)	−5~5 (deg.)
WISSDOM-lidar QVP	wind speed	-4~4 (m s^{-1})	−1~3 (m s^{-1})
	w-component winds	−0.8~0.8 (m s^{-1})	−0.2~0.6 (m s^{-1})

5. Sensitivity test with various datasets, data implementation and weighting coefficients

5.1 Impacts of various datasets (Experiment A)

In this section, the impacts of various datasets on data implemented in the WISSDOM synthesis were evaluated. In particular, the quantitative variances between each design, control run, sounding observations, and the QVP can be estimated. The basic setting of Experiment A took off several inputs from the WISSDOM control run (cf. Table 1) as four designs in Experiment A. The details of these four designs are summarized in Table 4 as the control run without the lidar observations (A-1), the control run without the AWS observations (A-2), the control run without the sounding observations (A-3) and the control run without the LDAPS data (A-4). The discrepancies of 3D winds were examined between the control run and each design in Experiment A. Since the environmental wind speed is nearly comprised of uniform westerlies in this event, the results only show the difference in u-component winds between control run and each design (A-1~A-4) in Fig. 12. An additional test was designed as only Doppler lidar data are used without other constraints from $J_6 \sim J_8$ (A-5) to evaluate the performances between the modified and original versions of WISSDOM.

Fig. 12a reveals the discrepancies in horizontal u-component winds at 800 m MSL as the A-1 is subtracted from the control run. This result reflects the impacts of lidar observations on the u-component winds in the WISSDOM synthesis. The most significant contributions from the

598   lidar observations are the high wind speed existing near the DGW site in a relatively narrow

599   valley. The mechanisms of the accelerated wind speed due to the channeling effect in this local

600   area were verified by our previous study (Tsai et al. 2022). The lidar observations also contributed

601   to the high wind speed in another area near the western side of the MHS site (128.68°E, 37.66°N).

602   Based on the analysis in the vertical cross section of u-component winds in A-1 (Fig. 12b), the

603   lidar observations significantly affected the high wind speed only in the lower levels (below ~900

604   m MSL) but not in the higher levels. Lidar observations provided sufficient coverage only for

605   lower levels and not higher levels (cf. Fig. 4).

606

Table 4 Experiment setting (sensitivity testing)

Control run	Various datasets	Including Doppler lidars, AWS, Soundings, LDAPS
	Interpolation of AWS	RI: 1.0 km, VE: 90%
	Weighting Coefficient	Doppler Lidars (α_1): 10^6 Background (α_2): 10^2 Sounding (α_6): 10^6 AWS (α_7): 10^6 LDAPS (α_8): 10^3
Experiment A	Various datasets	A-1 Excluding Doppler Lidars A-2 Excluding AWS A-3 Excluding Soundings A-4 Excluding LDAPS A-5 Only Doppler lidars
Experiment B	Interpolation of AWS	B-1 RI: 0.5 km, VE: 50% B-2 RI: 0.5 km, VE: 90% B-3 RI: 1.0 km, VE: 50% B-4 RI: 2.0 km, VE: 50% B-5 RI: 2.0 km, VE: 90%
Experiment C	Weighting Coefficient (constraints)	C-1 AWS (α_7): 10^3 C-2 Doppler Lidars (α_1): 10^3 C-3 LDAPS (α_8): 10^6

607

608   The impacts of the AWS cause negative values on the u-component winds in most areas at

609   800 m MSL in A-2 (Fig. 12c), especially in the western areas of the MHS site. Negative

610   contributions of the u-component winds produced by the AWS observations were restricted near

611   the surface, and the low wind speed area was extended to ~100 m above the surface (Fig. 12d).

612   The contributions of the u-component winds from the sounding observations were weak near the

613   DGW sounding site in A-3 (Figs. 12e and 12f). The impacts of u-component winds from the

614   LDAPS datasets were rather smaller in most of analysis area. in A-4 (Figs. 12g and 12h).

615   Relatively weak winds were presented near the surface from the results of A-5 (Figs. 12i and

616   12j). These results reflect that the additional constraints play crucial roles, especially at lower

617   layers. Furthermore, it is implied that the winds can be reasonably retrieved when additional

618   constraints are set in the modified version of WISSDOM.

619
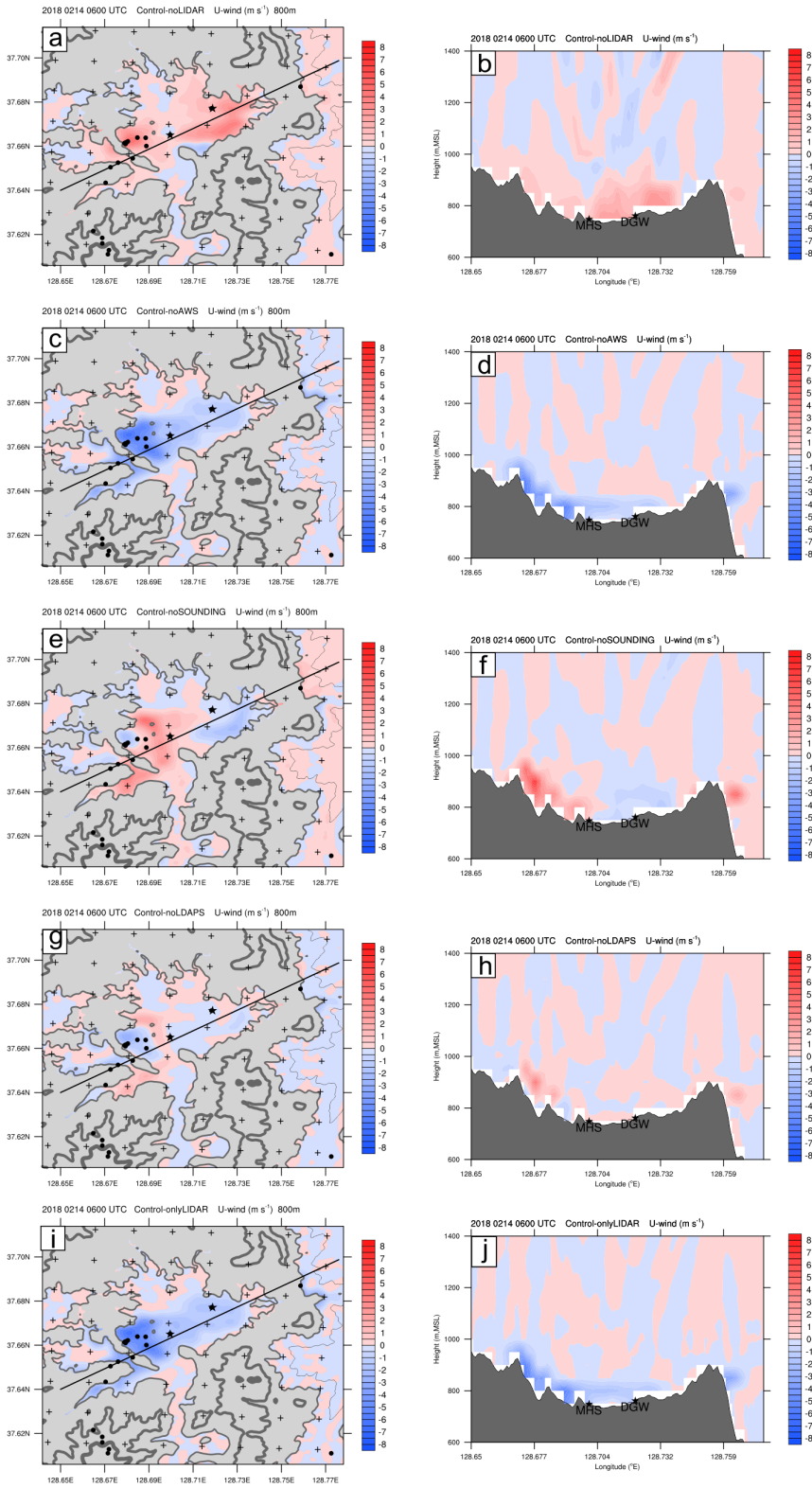
Figure 12. (a) The discrepancies in horizontal u-component winds between the control run and A-1 at 800 m MSL

at 06:00 UTC on 14 Feb. 2018. (b) The same as (a) but for the vertical section along the black line in (a). (c) and

(d) are the same as (a) and (b) but for A-2. (e) and (f) are the same as (a) and (b) but for A-3. (g) and (h) are the

same as (a) and (b) but for A-4. (i) and (j) are the same as (a) and (b) but for A-5.

624

625   Averaged discrepancies in derived 3D winds for each vertical level in entire domain are

626   shown in Fig. 13a. These results summarized a series of sensitivity tests if the WISSDOM

627   synthesis lacks certain data inputs (i.e., A-1~A-5 in Experiment A) for derived u-, v- and w-

628   component winds in the test domain. Overall, the maximum absolute value of averaged

629   discrepancies for Experiment A are smaller than approximately 0.5 m s^{-1}, which are the

630   discrepancies of the u-component winds for A-1 and A-2 located at 800 m MSL. Except for these

631   values, the values of the derived u-, v- and w-component winds for A-1~A-2 are approximately

632   smaller than 0.2 m s^{-1} from the surface up to the top in the test domain. Based on the results of

633   A-5, relatively stronger values of derived u-component (exceeded -0.4 m s^{-1} at lower layers) can

634   be obtained from the setting like old version of WISSDOM. The wind speed can be better

635   modulated in modified version of WISSDOM when the Doppler lidar observations were adopted.

636   In addition, the discrepancies in derived 3D winds between sounding observations and QVP

637   were also examined along the sounding tracks (Fig. 13b) and above the DGW site (Fig. 13c).

638   Sounding observations played an essential role in the derived winds along its tracks. The

639   maximum discrepancies of u- (v-) component winds are exceeded by approximately -2 (-1) m

640   s^{-1} if the WISSDOM synthesis lacks sounding observations. However, small discrepancies

641   (nearly 0 m s^{-1}) were presented when the sounding (lidar) data were (not) implemented at all

642   levels in A-1. The peaks in the discrepancies manifested the potential impacts from the lidar and

643   AWS. This may be a result of lidar (AWS) having relativity higher data coverage at ~1.4 (0.8)

644   km MSL (cf. Fig. 4). The maximum discrepancies between the derived winds and the QVP winds

645   are approximately -4 and 4 (-1 and 0) m s^{-1} associated with u-, v- (w-) component winds.

646   Generally, the results reveal similar trends in A-1~A-5, which also implies that all the inputs in

647   the WISSDOM synthesis are equally significant against the QVP. In summary, the results of this

648   experiment (cf. Fig. 13) show that the lidar, sounding, and AWS data are more critical inputs in

649   modified WISSDOM. Therefore, it will be beneficial if various inputs can be included in the

650   synthesis.
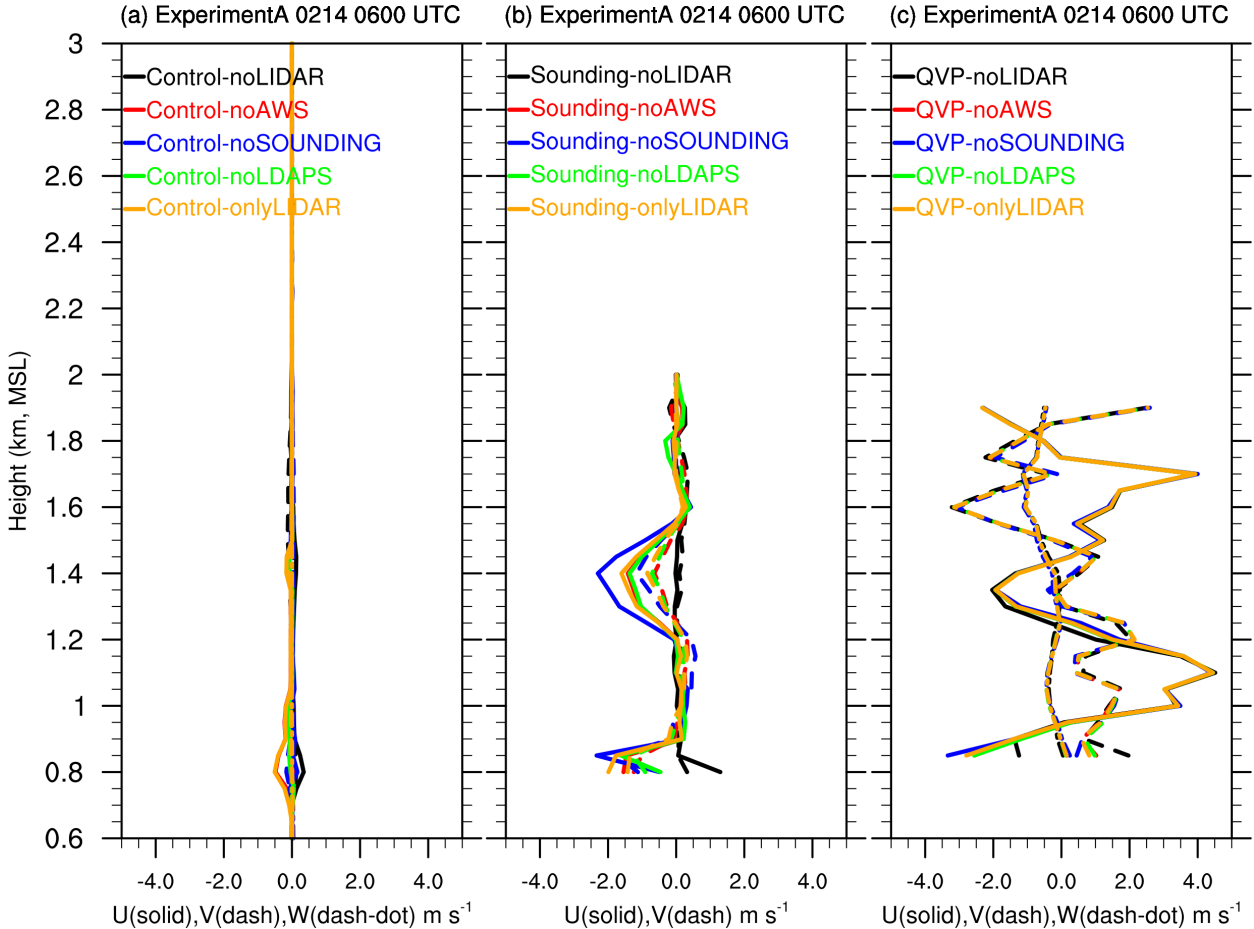
Figure 13. (a) Vertical profiles of averaged discrepancies of 3D winds for each design in Experiment A at 06:00 UTC on 14 Feb. 2018. The averaged discrepancies of u-, v- and w-component winds were plotted by solid, dash, and dash-dot lines, and the black, red, blue, green and orange lines indicate A-1, A-2, A-3, A-4 and A-5, respectively. (b) The same as (a) but for the discrepancies of sounding observations and u-, and v-component winds. (c) The same as (a) but for the discrepancies of QVP.

5.2 Radius of influence (RI) and vertical extension for the AWS (Experiment B)

Experiment B was performed to check the discrepancies in 3D winds between the control run and the different settings of RI and VE with the AWS observations. Because the average distance is approximately 0.1 to 2 km between each AWS site, there were five designs (B-1~B-5) in Experiment B with ranges of RI (VE) between 0.5 km (50%) and 2 km (90%). The details are shown in Table 4. The horizontal u-component winds at 800 m MSL and the vertical structure of Experiment B at one time step (06:00 UTC on 14 February 2018) are shown in Fig. 14. An unusual circular area with positive discrepancies around the MHS site was depicted in B-1 (Figs,

665   14a and 14b), which may have been produced by the insufficient RI distance and VE (the circular

666   artefact is removed when increasing VE to 90%). Relatively smaller RI and VE values can only

667   include relatively less wind information if the distances are large between each AWS. Enlarging

668   the RI and VE are required to appropriately include more wind information from the AWS

669   observations. Figs. 14c and 14d show the results of B-2 as VE reached 90%. Although the unusual

670   circle vanished, there were discontinuities with negative values near the northern and southern

671   areas of the MHS site and positive areas surrounding the AWS (128.68°E, 37.66°N). The setting

672   of B-3 was similar to that of the control run except that the VE was 50%. The discrepancies were

673   relatively small, albeit dense AWS contributed even smaller negative values in the western areas

674   of the MHS sites (Figs. 14g and 14h). Obviously, positive discrepancies appeared near the

675   northern and southern areas of the MHS site in B-4 and B-5 (Figs. 14g-j). The impacts of the

676   AWS with various settings (B-1~B-5) on the discrepancies in u-component winds were both

677   restricted near the surface, even with a larger RI and high VE.

678
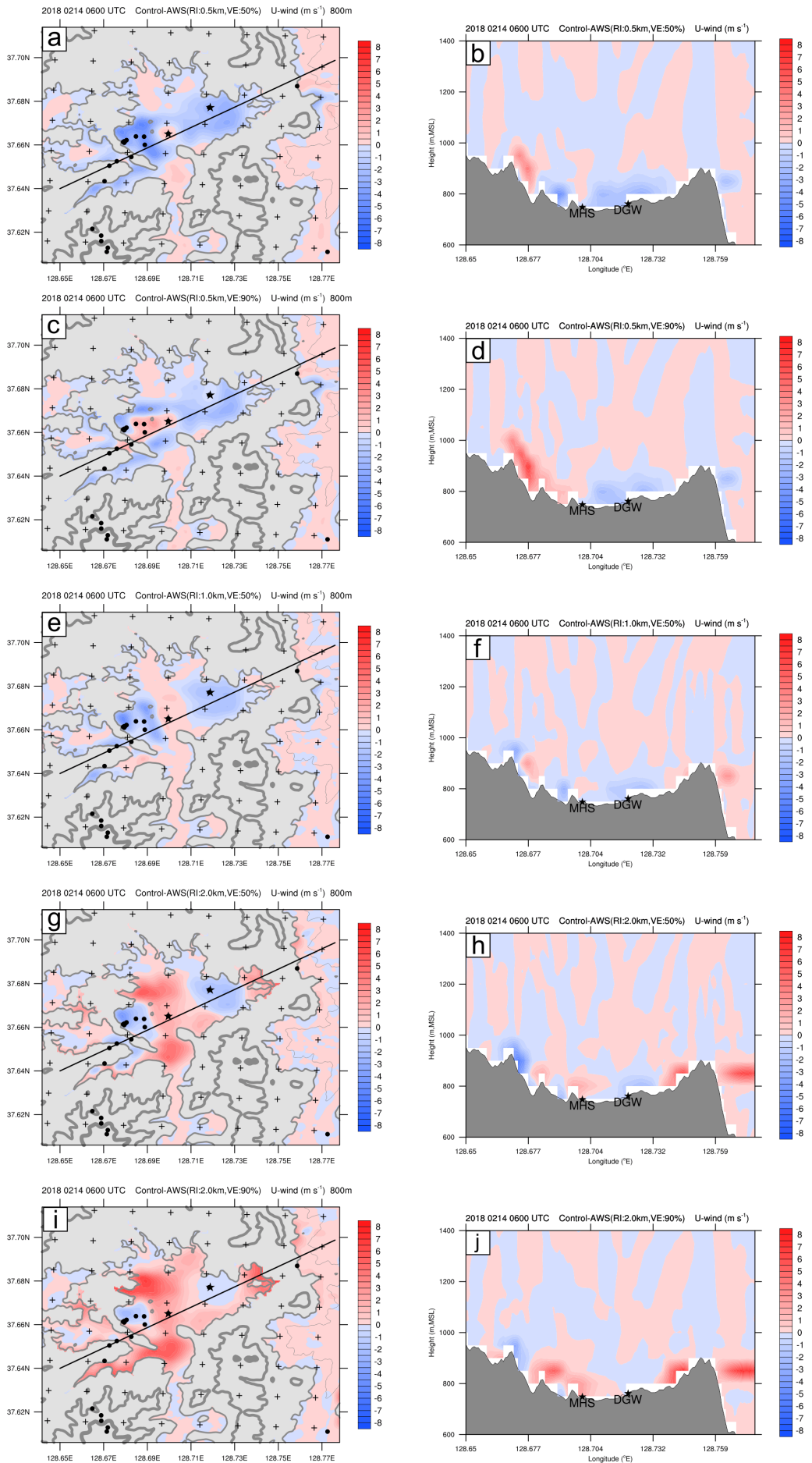
679 Figure 14. The same as Fig.12, but (a) and (b) for B-1. (c) and (d) are the same as (a) and (b) but for B-2. (e) and (f)

680   are the same as (a) and (b) but for B-3. (g) and (h) are the same as (a) and (b) but for B-4. (i) and (j) are the same

681   as (a) and (b) but for B-5.

682   Fig. 15a shows the vertical profiles of averaged discrepancies of derived 3D winds in

683 Experiment B. This figure summarizes the results of sensitivity testing with different settings of

684 the RI and VE in WISSDOM (i.e., B-1~B-5 in Experiment B, shown in Table 4) for derived u-,

685 v- and w-component winds in the test domain. The maximum discrepancies of u-component

686 winds in B-1, B-2 and B-3 were quite small at only 0.4, 0.3 and 0.2 m s^{-1}, respectively.

687 Nevertheless, the maximum discrepancies of u-component winds for B-4 and B-5 were larger

688 than 0.6 m s^{-1} and even exceeded ~1 m s^{-1}. Although the discrepancies in the u-component winds

689 in B-1 were small, the discrepancies in the v-component winds in B-1 reveal unusual patterns,

690 with larger positive values at ~1100 m MSL and negative values at ~1800 m MSL (black dashed

691 line in Fig. 15a), the possible reason is the minimizations of cost function are not converged well

692 because relatively few and weak v-component winds were included in B-1. Except for this value,

693 the maximum discrepancies of v-component winds were small for B-2~B-5, and the maximum

694 discrepancies of w-component winds were also small for all of Experiment B. Note that B-3

695 always has the smallest discrepancies with the derived 3D winds because the setting is quite

696 similar to the control run. Figs. 15b and 15c show the discrepancies of derived 3D winds between

697 the sounding observations and QVP. Their patterns are similar to A-1~A5 (cf. Figs. 13b and 13c),

698 except there were relatively larger values of u- (v-) component winds at lower layers

699 (approximately −3 and 1 m s^{-1}) in B-1 (Fig. 15b). The v-component winds also presented larger

700 values (exceeded ~3 m s^{-1}) below ~1.2 km MSL compared with the QVP (Fig. 15c). The

701 conclusions indicated that the moderate setting (i.e., RI is 1 km) would be helpful to obtain minor

702 differences with the control run, sounding observations and the QVP. On the other hand, the

703 limited setting in experiment B (i.e., B-1) was helpless. In addition, the wind directions and speed

704 should be dominated by terrain, and the implementation of AWS data is crucial for the modified

705 WISSDOM synthesis, especially in the lower layers.
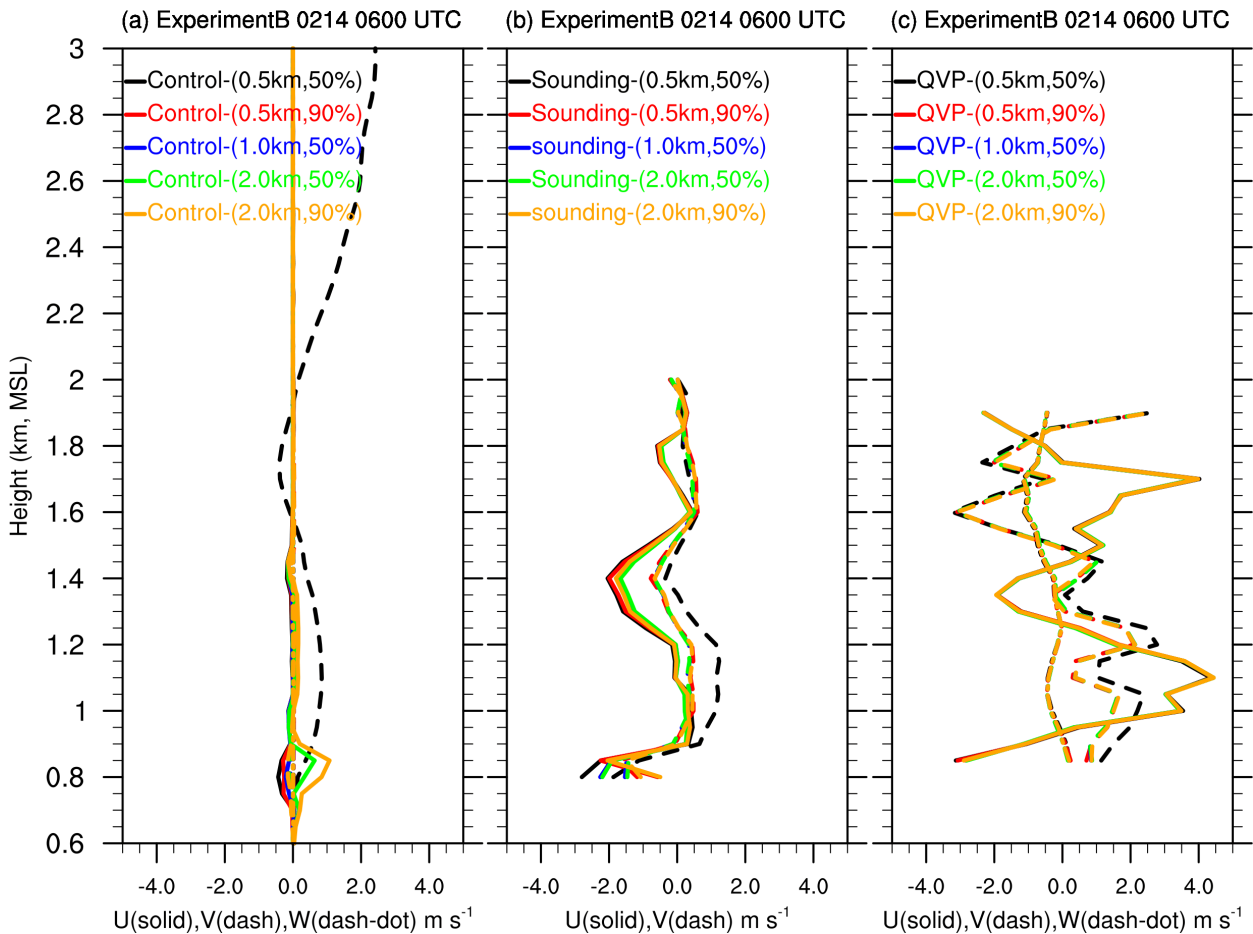
706

707 Figure 15. The same as Fig. 13. but for B-1~B-5.

5.3 Different weighting coefficients for the constraints (Experiment C)

709   Experiment C was designed to check the discrepancies in the derived u-component winds

710 between the control run and experimental runs with different weighting coefficients for each

711 constraint related to the AWS, lidar and LDAPS (corresponding to C-1, C-2 and C-3 in Table 4).

712 Originally, the weighting coefficients for the AWS and lidar observations were set to 10^6, and the

713 value was 10^3 for the LDAPS dataset (i.e., control run, Table 1). The results of Experiment C

714 show significant negative discrepancies in u-component winds near the surface in C-1, especially

715 in the areas next to the AWS (128.68°E, 37.66°N). The discrepancies for C-1 (Figs. 16a and 16b)

716 and C-2 (Figs. 16c and 16d) are similar to those for A-2 (Figs. 12c and 12d) and A-1 (Figs. 12a

717 and 12b), respectively. The inputs of AWS and lidar both contributed relatively weak impacts to

718   the WISSDOM synthesis when the weighting coefficient was set to 10^3. Irrational patterns were

719   depicted when the weighting coefficient of LDAPS inputs increased to 10^6, and larger and

720   positive discrepancies were crowded into most areas in the valley (i.e., C-3, Figs. 16e). Larger

721   and positive discrepancies existed only near the surface, and there were negative discrepancies

722   between approximately 1000 m and 1400 m (Fig. 16f). Notably, significant variances usually

723   existed between the observations and reanalysis datasets due to various spatiotemporal

724   resolutions. The results of scenario C-3 do not converge well because there was a relatively more

725   significant gradient between each input as their weighting coefficients were set to be the same

726   (i.e., 10^6). In this way, the effects of poor convergences might be amplified and superposed with

727   the AWS and lidar observations along the sounding tracks. This may be a possible reason that

728   artificial signals existed over the DGW site in scenario C-3.

729   The vertical profiles of averaged discrepancies of derived 3D winds in Experiment C are

730   shown in Fig. 17a. Absolute values of the discrepancies in the u-, v- and w-component winds are

731   smaller than 1 m s^{-1}, except for the discrepancies in the v-component winds with low weighting

732   of the AWS observations (i.e., C-1) and the discrepancies in the u- and v-component winds with

733   the high weighted LDAPS (i.e., C-3). The discrepancies in the v-component winds in C-1

734   exceeded -5 m s^{-1} at ~1100 m MSL and were larger than -15 m s^{-1} above 2600 m MSL. These

735   unreasonable characteristics are also shown as the discrepancies in the v-component winds in B-

736   1 (cf. Fig. 15a). The discrepancies in the u- and v-component winds in C-3 are 15 m s^{-1} and 4 m

737   s^{-1}, respectively, in the layers between 700 and 900 m MSL. Alternative positive and negative

738   discrepancies in the range of -3 to 3 m s^{-1} for the u-component winds in C-3 were found above

739   1000 m MSL.

740   The discrepancies in derived 3D winds between sounding observations and QVP in

741   Experiment C were also examined. Compared to the sounding observations, more significant

742   discrepancies in the u- and v-component winds (exceeded ~20 m s^{-1}) can be obtained when

743   reducing (increasing) the weighting coefficients of the AWS (LDAPS) data (Fig. 17b). However,

744   the impacts of lidar against the QVP are shown; their discrepancies are in the range of −1 to 2 m

745   s⁻¹ for the u-component winds in C-2 (Fig. 17c). The conclusions reveal that the weighting

746   coefficients of the AWS and LDAPS (lidar) are (moderately) significantly sensitive to the derived

747   winds. Therefore, the weighting coefficients of LDAPS and AWS are not necessarily changed

748   much.
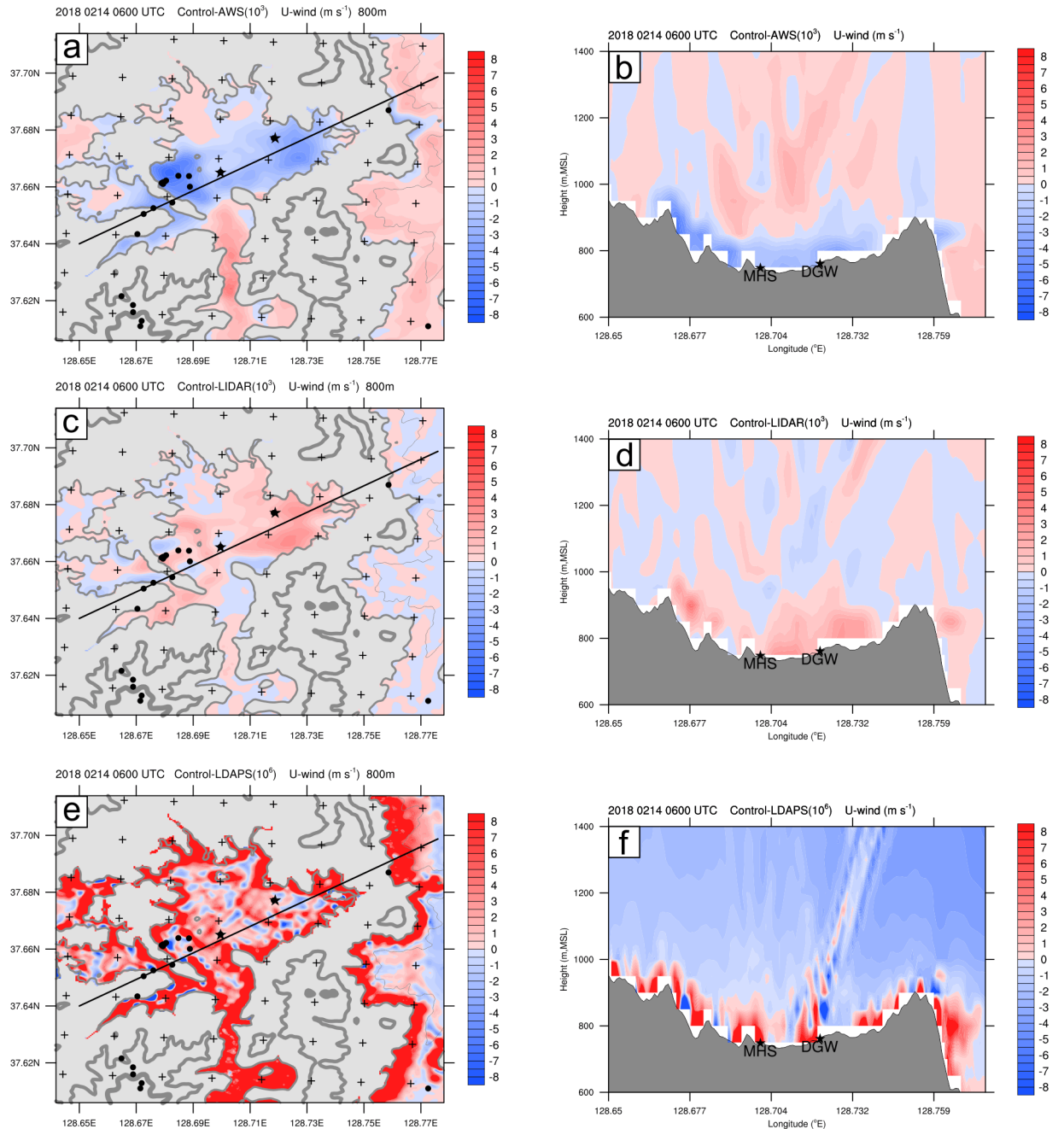
749

750   Figure 16. The same as Fig.12, but (a) and (b) for C-1. (c) and (d) are the same as (a) and (b) but for C-2. (e) and (f)

751   are the same as (a) and (b) but for C-3.
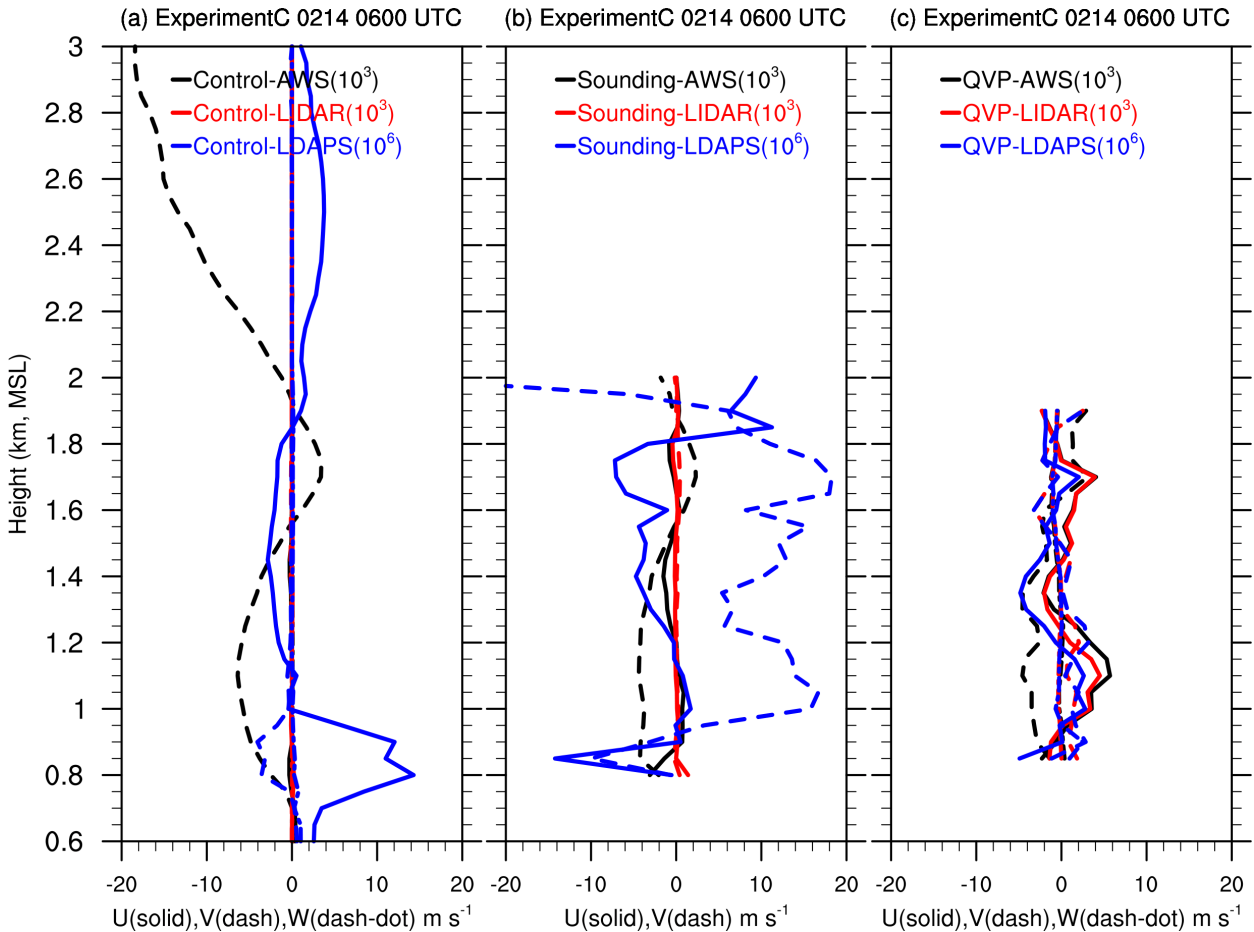
Figure 17. The same as Fig. 13 but for C-1~C-3.

6. Conclusion

A modified WISSDOM synthesis scheme was developed to derive high-quality 3D winds under clear-air conditions. The main difference from the original version is that multiple lidar observations were used, and high-resolution 3D winds (50 m horizontally and vertically) were first derived in the modified WISSDOM scheme. In addition, all available datasets were included as one of the constraints in the cost function in this study. The data implementation and the detailed principles of the modified WISSDOM were also elaborated. This modified WISSDOM scheme was performed over the TMR to retrieve 3D winds during a strong wind event during ICE-POP 2018. The performance was evaluated via a series of sensitivity tests and compared with conventional observations.

764   The intercomparisons of horizontal winds during the entire research period reveal a relatively

765   high correlation coefficient between the optimal results of WISSDOM synthesis and sounding's

766   u- (v-) component winds exceeding 0.97 (0.87) at the DGW site. Furthermore, the average bias

767   is −0.78 m s^{-1} (0.09 m s^{-1}), and the RMSD is 1.77 m s^{-1} (1.65 m s^{-1}) for the u- (v-) component

768   winds. The intercomparisons of 3D winds between the WISSDOM synthesis and lidar QVP also

769   showed a higher correlation coefficient (0.84) for u-component winds, but a relatively smaller

770   correlation coefficient remained at 0.35 for v-component winds in this strong wind event. The

771   average bias (RMSD) of u-component winds is 2.83 m s^{-1} (3.69 m s^{-1}), and the average bias and

772   RMSD of v-component winds are 2.26 m s^{-1} and 2.92 m s^{-1}, respectively (cf. Table 2). Chen

773   (2019) analyzed the correlations between 3D winds derived from radar and observations in

774   several typhoon cases; the mean correlation coefficient ranged from 0.56 to 0.86, and the RMSD

775   was between 1.13 and 1.74 m s^{-1}. Compared to their results, only u-component winds have

776   relatively higher correlation coefficients, but the RMSD values are slightly higher in this study,

777   which may have been caused by the high variability in westerly winds associated with the moving

778   LPS. The statistical error results of the winds between the optimal results of WISSDOM synthesis

779   and observations show a good performance of the retrieved 3D winds in this strong wind event

780   (Table 3). Generally, the median values of wind directions are within ~10 degrees. Compared

781   with lidar QVP (sounding observations) the median values of the wind speed are approximately

782   −1~3 m s^{-1} (−1~0.5 m s^{-1}) and the vertical velocity is within −0.2~0.6 m s^{-1}. Compared with

783   lidar QVP (sounding observations) above the DGW site, the interquartile range of wind directions

784   is −10~5 (0-2.5) degrees, the wind speed is approximately −4~4 m s^{-1} (−1~3 m s^{-1}) and the

785   vertical velocity is −0.8~0.8 m s^{-1}. The summaries of the correlation coefficients, average bias,

786   the RMSD, and range of statistical errors are shown in the schematic diagrams as Figs. 18a and

787   18b.
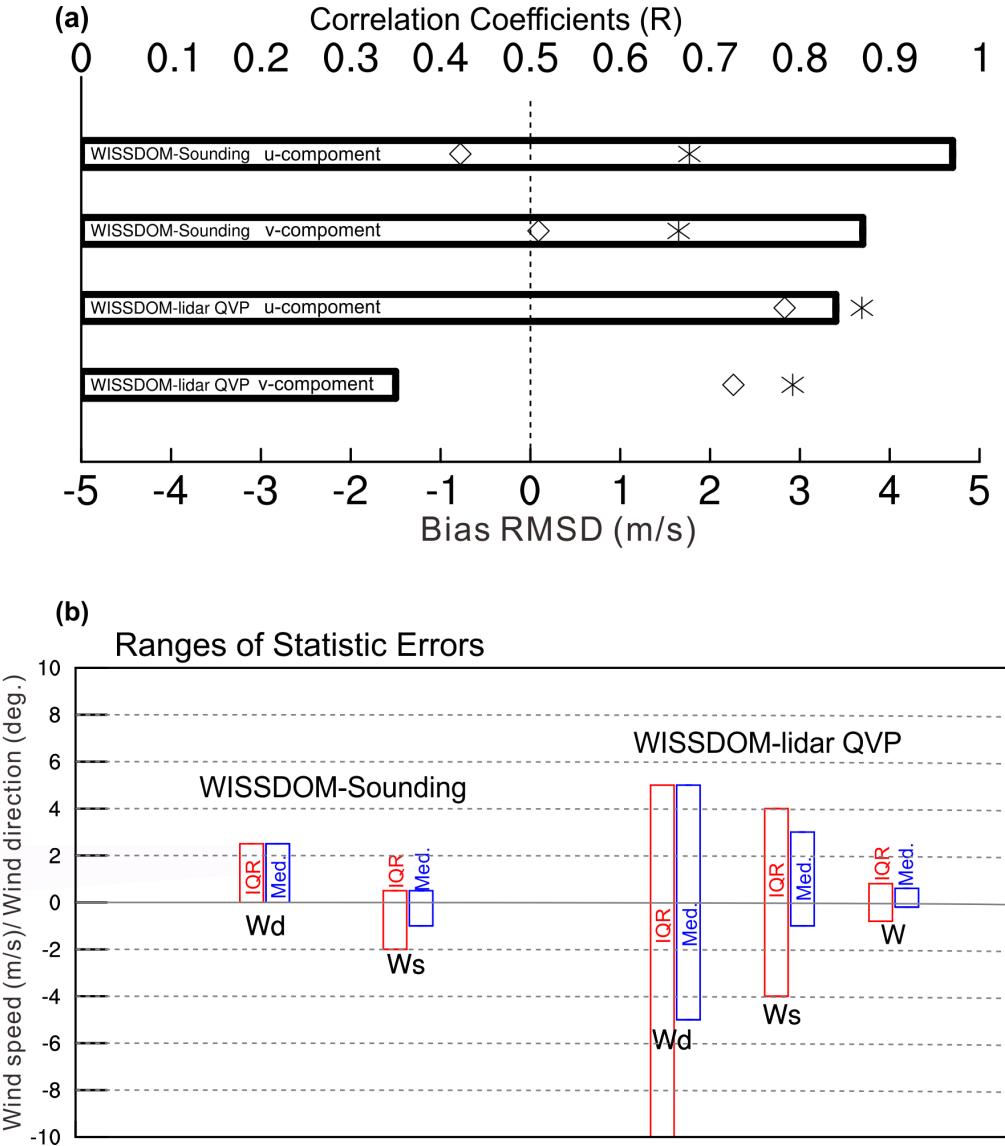
Figure 18. Schematic diagrams for the results of intercomparisons on (a) the correlation coefficients (R, histograms), the average bias (marked as diamonds), and the RMSD (marked as asterisks). (b) The ranges of statistic error for the IQR (red boxes) and median values (blue boxes). The wind directions, wind speed and w-component winds are denoted as Wd, Ws, and W respectively.

A control run (see the basic setting in Table 1) was set to explore the importance of acquired observation datasets, various distances of RI, VE from the AWS observations, and the weighting coefficient for each constraint (i.e., Experiments A-C, Table 4). The results of Experiment A show that the lidar and AWS play critical roles in the derived horizontal winds, and the lidars (AWS) provided positive (negative) contributions in stronger (weaker) wind speeds near the surface. The sounding and the LDAPS provided relatively smaller impacts on the derived horizontal winds from the WISSDOM synthesis. In Experiment B, minor discrepancies in 3D

800   winds were depicted when the RI (VE) was set to 1 km (50%), which indicated that the optimal

801   setting of the RI is 1 km. However, there were larger discrepancies in 3D winds (from -0.4 m s^{-1}

802   to ~1 m s^{-1}) when the RI was set at 0.5 km and 2 km, and the VE was set between 50% and 90%

803   (cf. Fig. 15). In Experiment C, significant discrepancies in 3D winds appeared by decreasing

804   (raising) the weighting coefficient from the AWS observations (LDPAS datasets). Relatively

805   reasonable winds can be derived with optimal settings in modified WISSDOM, and the setting

806   of 90% (50%) in VE is also recommended over complex terrain (flat surface). These sensitivity

807   tests will help verify the impacts against various scenarios and observational references in this

808   area. The conclusions can also be a good reference for deciding the best locations to deploy the

809   instruments.

810   This study demonstrated that reasonable patterns of 3D winds were derived by the modified

811   WISSDOM synthesis scheme in a strong wind event. Reasonable winds can be retrieved from

812   modified WISSDOM with sufficient coverage from the data, a moderate weighting function, and

813   appropriate implementation from different datasets. In the future, many cases are required to

814   check the performance of this modified WISSDOM scheme with different synoptic weather

815   systems under clear-air conditions in different seasons. In addition, knowing the detailed

816   kinematic fields will help us to identify where the flow accelerates/decelerates over complex

817   terrain. Thus, the possible mechanisms of extremely strong winds in South Korea will be well

818   documented through combinations with derived dynamic fields (Tsai et al., 2018, 2022),

819   thermodynamic fields (Liou et al., 2019), observations and simulations. The detailed wind

820   structures can be well documented for any meteorological phenomena in clear-air conditions

821   (e.g., land−sea breezes, microdownbursts, nonprecipitation low-pressure systems, etc.) via a

822   modified version of WISSDOM. It also has broad applications in site surveys of wind turbines,

823   wind energy, monitoring wildfires, outdoor sports in mountain ranges, and aviation security.

Code and data availability. The scanning Doppler lidars, AWS, and sounding data used in this study are available through zenodo: https://doi.org/10.5281/zenodo.6537507. The LDAPS dataset is freely available from the KMA website (https://data.kma.go.kr).

Acknowledgments. This work was supported by the National Research Foundation of Korea (NRF) grant funded by the Korea government (MSIT) (No. 2021R1A4A1032646) and by the Korea Meteorological Administration Research and Development Program under Grant KMI2022-00310.

Author contributions. This work was made possible by contribution from all authors. Conceptualization, CLT, GWL; methodology, CLT, YCL, and KK; software, CLT, YCL, and KK; validation, KK, YCL, and GWL; formal analysis, CLT, and KK; investigation, CLT, and GWL; writing—original draft preparation, CLT; writing—review and editing, GWL, YCL and KK; visualization, CLT; supervision, GWL; funding acquisition, GWL. All authors have read and agreed to the published version of the manuscript.

Competing interests. The authors declare that they have no conflict of interest.

Special issue statement. This article is part of the special issue "Winter weather research in complex terrain during ICE-POP 2018 (International Collaborative Experiments for Pyeongchang 2018 Olympic and Paralympic winter games) (ACP/AMT/GMD inter-journal SI)". It is not associated with a conference.

References

Armijo, L.: A theory for the determination of wind and precipitation velocities with Doppler radars. J. Atmos. Sci., 26, 570–573. 1969.

Bell, M. M., Montgomery, M. T., and Emanuel, K. A.: Air–sea enthalpy and momentum exchange at major hurricane wind speeds observed during CBLAST, *J. Atmos. Sci.*, **69**, 3197–3222, https://doi.org/10.1175/JAS-D-11-0276.1, 2012.

Bell, T. M., Klein, P., Wildmann, N., and Menke, R.: Analysis of flow in complex terrain using multi-Doppler lidar retrievals, *Atmos. Meas. Tech.*, **13**, 1357–1371, https://doi.org/10.5194/amt-13-1357-2020, 2020.

Browning, K. A., and Wexler, R..: The Determination of Kinematic Properties of a Wind Field Using Doppler Radar, *J. Appl. Meteorol.*, **7**, 105–113, https://doi.org/10.1175/1520-0450(1968)007<0105:TDOKPO>2.0.CO;2, 1968.

Chen, Y.-A.: Verification of multiple-Doppler-radar derived vertical velocity using profiler data and high resolution examination over complex terrain, M.S. thesis, National Central University, 91 pp., 2019.

Choi, D., Hwang, Y., Lee, YH.: Observing Sensitivity Experiment Based on Convective Scale Model for Upper-air Observation Data on GISANG 1 (KMA Research Vessel) in Summer 2018. *Atmosphere*, **30**, 17–30, 2020 (Korean with English abstract).

Cha, T.-Y. and Bell, M. M.: Comparison of single-Doppler and multiple-Doppler wind retrievals in Hurricane Matthew (2016), *Atmos. Meas. Tech.*, **14**, 3523–3539, https://doi.org/10.5194/amt-14-3523-2021, 2021.

Choukulkar, A., Brewer, W. A., Sandberg, S. P., Weickmann, A., Bonin, T. A., Hardesty, R. M., Lundquist, J. K., Delgado, R., Iungo, G. V., Ashton, R., Debnath, M., Bianco, L., Wilczak, J. M., Oncley, S., and Wolfe, D.: Evaluation of single and multiple Doppler lidar techniques to measure complex flow during the XPIA field campaign, *Atmos. Meas. Tech.*, **10**, 247–264, https://doi.org/10.5194/amt-10-247-2017, 2017.

874   Colle, B. A., and Mass, C. F.: High-Resolution Observations and Numerical Simulations of

875   Easterly Gap Flow through the Strait of Juan de Fuca on 9–10 December 1995. *Mon. Wea.*

876   *Rev.*, **128**, 2398–2422,

877   Cressman, G. P.: An operational objective analysis system. *Mon. Wea. Rev.*, **87**, 367–374, 1959.

878   Gao, J., Droegemeier, K. K., Gong, J., and Xu, Q.: A method for retrieving mean horizontal wind

879   profiles from single-Doppler radar observations contaminated by aliasing, *Mon. Wea.*

880   *Rev.*,   **132**,   1399–1409,   https://doi.org/10.1175/1520-

881   0493(2004)132<1399:AMFRMH>2.0.CO;2, 2004.

882   Hill, M., R. Calhoun, H. J. S. F., Wieser, A., Dornbrack, A., Weissmann, M., Mayr, G., and

883   Newsom, R.: Coplanar Doppler lidar retrieval of rotors from T-REX, *J. Atmos. Sci.*, **67**,

884   713–729, 2010.

885   Jou, B. J.-D., Lee, W.-C., Liu, S.-P., and Kao, Y.-C.: Generalized VTD retrieval of atmospheric

886   vortex kinematic structure. Part I: Formulation and error analysis, *Mon. Weather Rev.*,

887   **136**, 995–1012, https://doi.org/10.1175/2007MWR2116.1, 2008.

888   Kim D.-J., Kang G., Kim D.-Y., Kim J.-J.: Characteristics of LDAPS-Predicted Surface Wind

889   Speed and Temperature at Automated Weather Stations with Different Surrounding Land

890   Cover   and   Topography   in   Korea. *Atmosphere*,   **11**,   1224.

891   https://doi.org/10.3390/atmos11111224, 2020.

892   Kim, J.-H., R. D. Sharman, R. D., Benjamin, S., Brown, J., Park, S.-H. and Klemp, J.:

893   Improvement of Mountain Wave Turbulence Forecast in the NOAA's Rapid Refresh

894   (RAP) Model with Hybrid Vertical Coordinate System, *Weather Forecast*, **34(6)**, 773-

895   780, https://doi.org/10.1175/WAF-D-18-0187.1, 2019.

896   Kim, K., Lyu, G., Baek, S., Shin, K., and Lee, G.: Retrieval and Accuracy Evaluation of

897   Horizontal Winds from Doppler Lidars during ICE-POP 2018, *Atmos.*, **32**, 163–178,

898   https://doi.org/10.14191/Atmos.2022.32.2.161, 2022.

899   Lee, J., Seo, J., Baik, J., Park, S., and Han, B.: A Numerical Study of Windstorms in the Lee of

the Taebaek Mountains, South Korea: Characteristics and Generation Mechanisms. *Atmosphere*, **11**, 431. https://doi.org/10.3390/atmos11040431, 2020.

Lee, J.- T., Ko, K.- Y., Lee, D.- I., You, C.- H., and Liou, Y.- C.: Enhancement of orographic precipitation in Jeju Island during the passage of Typhoon Khanun (2012), *Atmos. Res.*, **201**, 1245–1254. https://doi.org/10.1016/j.atmosres.2017.10.013, 2017.

Lee, W.-C., Marks, F. D., and Carbone, R. E.: Velocity track display – A technique to extract real-time tropical cyclone circulations using a single airborne Doppler radar, *J. Atmos. Ocean. Tech.*, **11**, 337–356, https://doi.org/10.1175/1520-0426(1994)011<0337:VTDTTE>2.0.CO;2, 1994

Lee, W.-C., Jou, B. J.-D., Chang, P.-L., and Deng, S.- M.: Tropical cyclone kinematic structure derived from single-Doppler radar observations. Part I: Interpretation of Doppler velocity patterns and the GBVTD technique, *Mon. Weather Rev.*, **127**, 2419–2439, https://doi.org/10.1175/1520-0493(1999)127<2419:TCKSRF>2.0.CO;2, 1999.

Liou, Y.-C., Wang, T.-C. C., Lee, W.-C., and Chang, Y.-J.: The retrieval of asymmetric tropical cyclone structures using Doppler radar simulations and observations with the extended GBVTD technique, *Mon. Weather Rev.*, **134**, 1140–1160, https://doi.org/10.1175/MWR3107.1, 2006.

Liou, Y., and Chang, Y.: A Variational Multiple–Doppler Radar Three-Dimensional Wind Synthesis Method and Its Impacts on Thermodynamic Retrieval. *Mon. Wea. Rev.*, **137**, 3992–4010, https://doi.org/10.1175/2009MWR2980.1, 2009.

Liou, Y., Chang, S., and Sun, J.: An Application of the Immersed Boundary Method for Recovering the Three-Dimensional Wind Fields over Complex Terrain Using Multiple-Doppler Radar Data. *Mon. Wea. Rev.*, **140**, 1603–1619, https://doi.org/10.1175/MWR-D-11-00151.1, 2012.

Liou, Y., Chen Wang, T., Tsai, Y., Tang, Y., Lin, P., and Lee, Y.: Structure of precipitating systems over Taiwan's complex terrain during Typhoon Morakot (2009) as revealed by weather

926   radar and rain gauge observations, *J. Hydrology*, **506**, 14-25.

927   https://doi.org/10.1016/j.jhydrol.2012.09.004, 2013.

928 Liou, Y., Chiou, J., Chen, W., and Yu, H.: Improving the Model Convective Storm Quantitative

929   Precipitation Nowcasting by Assimilating State Variables Retrieved from Multiple-

930   Doppler Radar Observations. *Mon. Wea. Rev.*, **142**, 4017–4035,

931   https://doi.org/10.1175/MWR-D-13-00315.1, 2014.

932 Liou, Y., Chen Wang, T., and Huang, P.: The Inland Eyewall Reintensification of Typhoon

933   Fanapi (2010) Documented from an Observational Perspective Using Multiple-Doppler

934   Radar and Surface Measurements. *Mon. Wea. Rev.*, **144**, 241–261,

935   https://doi.org/10.1175/MWR-D-15-0136.1, 2016.

936 Liou, Y. C., Yang, P. C., and Wang, W. Y.: Thermodynamic recovery of the pressure and

937   temperature fields over complex terrain using wind fields derived by multiple-Doppler

938   radar synthesis. Mon. Wea. Rev., **147(10)**, 3843-3857, https://doi.org/10.1175/MWR-D-

939   19-0059.1, 2019.

940 Mass, C. F., and Ovens, D.: The Northern California Wildfires of 8–9 October 2017: The Role

941   of a Major Downslope Wind Event. *Bull. Amer. Meteor. Soc.*, **100**, 235–256,

942   https://doi.org/10.1175/BAMS-D-18-0037.1, 2019.

943 Mohr, C. G., and Miller, L. J. : CEDRIC—A software package for Cartesian Space Editing,

944   Synthesis, and Display of Radar Fields under Interactive Control. Preprints, *21st Conf. on*

945   *Radar Meteorology,* Edmonton, AB, Canada, Amer. Meteor. Soc., 569–574, 1983.

946 Oue, M., Kollias, P., Shapiro, A., Tatarevic, A., and Matsui, T.: Investigation of observational

947   error sources in multi-Doppler-radar three-dimensional variational vertical air motion

948   retrievals, *Atmos. Meas. Tech.*, **12**, 1999–2018, https://doi.org/10.5194/amt-12-1999-

949   2019, 2019.

950 Park, J.-R., Kim, J.-H., Shin, Y., Kim, S.-H., Chun, H.-Y., Jang, W., Tsai, C.-L. and Lee, G.: A

951   numerical simulation of a strong windstorm event in the Taebaek Mountain Region in

Korea during the ICE-POP 2018, *Atmos. Res.*, **272**, 106158, https://doi.org/10.1016/j.atmosres.2022.106158.

Päschke, E., Leinweber, R., and Lehmann, V.: An assessment of the performance of a 1.5 μm Doppler lidar for operational vertical wind profiling based on a 1-year trial, *Atmos. Meas. Tech.*, **8**, 2251–2266, https://doi.org/10.5194/amt-8-2251-2015, 2015.

Reed, T. R.: GAP WINDS OF THE STRAIT OF JUAN DE FUCA. *Mon. Wea. Rev.*, **59**, 373–376, https://doi.org/10.1175/15200493(1931)59<373:GWOTSO>2.0.CO;2, 1931.

Ryzhkov, A., Zhang, P., Reeves, H., Kumjian, M., Tschallener, T., Trömel, S., and Simmer, C.: Quasi-Vertical Profiles—A New Way to Look at Polarimetric Radar Data. *J. Atmos. Oceanic Technol.*, **33**, 551–562, https://doi.org/10.1175/JTECH-D-15-0020.1, 2016.

Tsai, C., Kim, K., Liou, Y., Lee, G., and Yu, C.: Impacts of Topography on Airflow and Precipitation in the Pyeongchang Area Seen from Multiple-Doppler Radar Observations. *Mon. Wea. Rev.*, **146**, 3401–3424, https://doi.org/10.1175/MWR-D-17-0394.1, 2018.

Tsai, C.-L., Kim, K., Liou, Y.-C., Kim, J.-H., Lee, Y., and Lee, G.: Orographic-induced strong wind associated with a low-pressure system under clear-air condition during ICE-POP 2018, *J. Geophys. Res. Atmos.*, **127**, e2021JD036418. https://doi.org/10.1029/2021JD036418, 2022.

Tseng, Y., and Ferziger, J.: A ghost-cell immersed boundary method for flow in complex geometry. *J. Comput. Phys.*, **192**, 593–623, https://doi.org/10.1016/j.jcp.2003.07.024. 2003.

Yu, C.- K., and Bond, N. A.: Airborne Doppler observations of a cold front in the vicinity of Vancouver Island. Mon. Wea. Rev., 130, 2692-2708, https://doi.org/10.1175/1520-0493(2000)128<1577:ADOOAL>2.0.CO;2, 2002.

Yu, C., and Tsai, C.-L.: Surface Pressure Features of Landfalling Typhoon Rainbands and Their Possible Causes. *J. Atmos. Sci.*, **67**, 2893–2911, https://doi.org/10.1175/2010JAS3312.1,

978   2010.

979   Yu, C.-K., and Tsai, C.-L. : Structural and surface features of arc-shaped radar echoes along an

980   outer tropical cyclone rainband. *J. Atmos. Sci.*, **70**, 56– 72. https://doi.org/10.1175/JAS-

981   D-12-090.1, 2013.

982   Yu, C.-K., and Tsai, C.-L.: Structural changes of an outer tropical cyclone rain band encountering

983   the topography of northern Taiwan. *Q. J. R. Meteorol. Soc*, **143**, 1107–1122.

984   https://doi.org/10.1002/qj.2994, 2017.

985   Yu, C.- K., and Jou, B. J.-D.: Radar observations of diurnally forced, offshore convective lines

986   along the southeastern coast of Taiwan. Mon. Wea. Rev., 133, 1613-1636,

987   https://doi.org/10.1175/MWR2937.1, 2005.

988   Yu, C.-K., Cheng, L.-W., Wu, C.-C., and Tsai, C.-L.: Outer Tropical Cyclone Rainbands

989   Associated with Typhoon Matmo (2014). *Mon. Wea. Rev.*, **148**, 2935–2952,

990   https://doi.org/10.1175/MWR-D-20-0054.1, 2020.